remote sensing

MDPI

Article

Improved Global Gross Primary Productivity Estimation by Considering Canopy Nitrogen Concentrations and Multiple Environmental Factors

Helin Zhang [1,2], Jia Bai [1,2], Rui Sun [1,3,*], Yan Wang [4], Yuhao Pan [5,6], Patrick C. McGuire [7] and Zhiqiang Xiao [1]

1 State Key Laboratory of Remote Sensing Science, Faculty of Geographical Science, Beijing Normal University, Beijing 100875, China
2 Beijing Engineering Research Center for Global Land Remote Sensing Products, Faculty of Geographical Science, Beijing Normal University, Beijing 100875, China
3 Faculty of Arts and Sciences, Beijing Normal University, Zhuhai 519087, China
4 Department of Land Surveying and Geo-Informatics, The Hong Kong Polytechnic University, Hong Kong, China
5 Key Laboratory of Digital Earth Science, Aerospace Information Research Institute, Chinese Academy of Sciences, Beijing 100094, China
6 University of Chinese Academy of Sciences, Beijing 100049, China
7 Department of Meteorology, National Centre for Atmospheric Science, University of Reading, Reading RG6 7BE, UK
* Correspondence: sunrui@bnu.edu.cn

Abstract: The terrestrial gross primary productivity (GPP) plays a crucial role in regional or global ecological environment monitoring and carbon cycle research. Many previous studies have produced multiple products using different models, but there are still significant differences between these products. This study generated a global GPP dataset (NI-LUE GPP) with 0.05° spatial resolution and at 8 day-intervals from 2001 to 2018 based on an improved light use efficiency (LUE) model that simultaneously considered temperature, water, atmospheric CO_2 concentrations, radiation components, and nitrogen (N) index. To simulate the global GPP, we mapped the global optimal ecosystem temperatures (T_{opt}^{eco}) using satellite-retrieved solar-induced chlorophyll fluorescence (SIF) and applied it to calculate temperature stress. In addition, green chlorophyll index (CI_{green}), which had a strong correlation with the measured canopy N concentrations (r = 0.82), was selected as the vegetation index to characterize the canopy N concentrations to calculate the spatiotemporal dynamic maximum light use efficiency (ε_{max}). Multiple existing global GPP datasets were used for comparison. Verified by FLUXNET GPP, our product performed well on daily and yearly scales. NI-LUE GPP indicated that the mean global annual GPP is 129.69 ± 3.11 Pg C with an increasing trend of 0.53 Pg C/yr from 2001 to 2018. By calculating the SPAtial Efficiency (SPAEF) with other products, we found that NI-LUE GPP has good spatial consistency, which indicated that our product has a reasonable spatial pattern. This product provides a reliable and alternative dataset for large-scale carbon cycle research and monitoring long-term GPP variations.

Keywords: gross primary production (GPP); nitrogen (N); carbon dioxide (CO_2); environmental factors; light use efficiency (LUE)

Citation: Zhang, H.; Bai, J.; Sun, R.; Wang, Y.; Pan, Y.; McGuire, P.C.; Xiao, Z. Improved Global Gross Primary Productivity Estimation by Considering Canopy Nitrogen Concentrations and Multiple Environmental Factors. *Remote Sens.* **2023**, *15*, 698. https://doi.org/10.3390/rs15030698

Academic Editor: Yongze Song

Received: 21 November 2022
Revised: 19 January 2023
Accepted: 20 January 2023
Published: 24 January 2023

1. Introduction

The total atmospheric carbon dioxide (CO_2) assimilated by vegetation is known as gross primary productivity (GPP) and is generally considered the most significant carbon flux in the carbon cycle of terrestrial ecosystems, which plays an important role in global carbon and the climate system [1,2]. Especially in the background of rapid global climate change, accurate estimation of GPP is particularly essential and urgent [3].

The flux observation network based on the eddy covariance technique supplies lots of observational data (such as FLUXNET, Ameriflux, and Chinaflux), which have been used by a large number of studies as standard ground data [4–6]. However, due to the finite number and non-uniform distribution of sites, it is still unable to meet the needs of vegetation-productivity monitoring and evaluation at the larger scales [7]. In recent years, many studies have developed multifarious models including meteorological-based models [8,9], process-based models [10–13], light use efficiency (LUE) models [3,14–20], and data-driven models [21–24] to quantify GPP at different scales based on remote sensing data. Among these models, the LUE model has wide utilization due to its high accuracy, simple form and easy access to the input data [3,25,26]. However, the interannual variability of GPP estimated by the LUE models still deviates considerably from in situ observations [26,27]. Stocker et al. [28] suggested that one of the main reasons for the uncertainty in the GPP estimation is that the effects of environmental factors on photosynthesis are not fully incorporated into the LUE model.

Typically, GPP can be calculated using the LUE model as described in Equation (1):

$$GPP = \varepsilon_{max} \times APAR \times f(stress) \quad (1)$$

where the ε_{max} and APAR are the maximum LUE and the absorbed photosynthetically active radiation, respectively. The f ($stress$) represents the environmental factor used to adjust the ε_{max}. Among all environmental factors, temperature has an important influence on enzyme activity and electron transport rate, and a sufficient water supply ensures stomatal openness and physiochemical reactions in plants, which are the most common environmental stress factors in the LUE models [25,29]. However, most LUE models set the temperature parameter as a constant for each vegetation type, which ignores the spatial differences in the influence of temperature [30–32].

In recent years, several studies have proposed methods to calculate optimal temperatures [30,33,34], and Huang et al. [34] have published the first global map of optimal ecosystem temperatures (T_{opt}^{eco}), which may help to reduce the large uncertainty in GPP estimates due to temperature parameters. In situ GPP allows the estimation of site optimum temperatures, while at the regional scale, satellite-retrieved solar-induced chlorophyll fluorescence (SIF) capable of observing vegetation photosynthesis may be a better option than the traditional vegetation indices used in previous studies. Moreover, atmospheric CO_2 can diffuse through stomata into leaves and is a crucial driver of photosynthesis. Since the 1980s, global atmospheric CO_2 concentrations have increased by approximately 23%, contributing to increased photosynthesis and GPP. Although many studies have recognized the importance of the CO_2 fertilization effect, it has not been integrated into most LUE models, except for CFix [35], P-model [36], revised EC-LUE [26], PRELES model [37], and the Dry Matter Productivity (DMP) of the Copernicus global land service, which could result in the insensitivety of the GPP estimates to the increasing CO_2 concentrations. In addition, sunlit leaves are more likely to reach light saturation due to the simultaneous reception of direct and diffuse radiation [3,14,38]. So far, the impact of the radiation component on LUE has been agreed in many studies [3,14,19,26,39].

Nitrogen (N) is one of the most important components of enzymes and pigments and plays a crucial role in photosynthesis, which has not been considered in almost all LUE models [40–42]. In LUE models, the ε_{max} is assumed to be a constant value for each vegetation type, but it should be dynamic under various environmental conditions [43,44]. Many studies found that the ε_{max} is linearly related to canopy N concentrations and that the ε_{max} increases with increasing N deposition [45,46]. Therefore, introducing canopy N concentrations into the LUE model to calculate the ε_{max} with seasonal variation may make the LUE model more suitable for the actual situation of leaves adapting to environmental conditions changes [47].

The currently available canopy or leaf N products were compressed to a static value that lacked temporal variation and cannot reflect changes in the ε_{max} [41,48,49]. Furthermore, there may be high uncertainties and errors in canopy N content simulations based on

radiative transfer models due to their complex parameters and calculation processes [50]. In recent years, several vegetation indices based on satellite or in situ measurements of reflectance have been developed to estimate canopy N concentrations at local scales due to their simple calculations and high accuracy [40,50–53]. Therefore, calculating the ε_{max} using the vegetation index characterizing canopy N concentrations not only introduces N into the LUE model, but also enables the dynamic ε_{max}, which may have implications on the GPP simulation and facilitate the evaluation of the long-term impacts of N deposition on GPP.

In this study, an LUE model (NI-LUE) that integrated temperature, water, radiation components, CO_2 fertilization effects, and N was developed. In this model, a vegetation index capable of characterizing canopy N concentrations was selected to achieve dynamic ε_{max}. In addition, global T_{opt}^{eco} distribution mapped based on satellite-retrieved SIF were introduced to calculate the temperature stress factor. Our primary aim is to estimate global GPP and produce a novel dataset (0.05°, 8 days). We validated and evaluated our product using in situ observations at daily and annual scales. Moreover, multiple existing global GPP products were collected to indicate the effectiveness of the interannual variation and spatial distribution of our products.

2. Data

2.1. Site Data

The FLUXNET2015 dataset (https://FLUXNET.fluxdata.org/ (accessed on 11 October 2022)) includes carbon flux and other meteorological variables over 200 sites globally. In this study, we obtained daily GPP based on the nighttime partitioning method (GPP_NT_VUT_REF) along with meteorological variables including incident shortwave radiation (SW), air temperature (T_a), vapor pressure deficit (VPD), latent heat flux (LE), and sensible heat flux (H) for parameterizing model and validating the product. We chose high-quality data with a quality flag above 0.8 and deleted the negative GPP values. Firstly, we aggregated the daily values to 8-day time steps to match the leaf area index (LAI) product. Then, we verified the homogeneity of the flux sites within 5 km using high spatial resolution images. Finally, we selected 104 sites where the land cover type is consistent with the moderate-resolution imaging spectroradiometer (MODIS) land cover product (MCD12Q1), including 12 vegetation types: evergreen needleleaf forest (ENF), evergreen broadleaf forest, deciduous needleleaf forest (DNF), deciduous broadleaf forest (DBF), mixed forest (MF), closed shrubland (CSH), open shrubland (OSH), woody savanna (WSAV), savanna (SAV), grassland (GRA), permanent wetland (WET), and cropland (CRO). The location information of these sites is shown in Table A4.

To corroborate the ability of the selected vegetation index to characterize canopy N concentrations, we collected canopy mean N concentrations measurements from previous studies that had time stamps (Table A2). The canopy N concentrations were determined by the mean of dry-mass-based foliar N concentrations for all species in multiple field plots within each site. For detailed measurements of the canopy N concentration, please refer to Ollinger et al. [53] and Ollinger and Smith [54].

2.2. Global Scale Data

Here, we used the Global land surface satellite (GLASS) Advanced Very High Resolution Radiometer (AVHRR) LAI product (0.05° and 8-day) from 2001 to 2018 as vegetation structure parameters to drive the models and used it to decompose the APAR into the APAR of shaded leaves ($APAR_{sh}$) and sunlit leaves ($APAR_{su}$) [55] (http://www.glass.umd.edu/LAI/AVHRR/ (accessed on 11 October 2022)).

The NOAA Earth System Research Laboratory (ESRL) provided global three-hourly distributions of CO_2 mole fraction with 3° × 2° spatial resolution [56]. This study obtained CO_2 mole fraction data files for CT2019B from 2000 to 2018 and aggregated them into daily CO_2 concentrations, which were used to calculate the CO_2 fertilization effect in the

model. This dataset is available at https://gml.noaa.gov/aftp/products/carbontracker/co2/molefractions/co2_total/ (accessed on 11 October 2022).

ERA-5 is a reanalysis dataset produced by the European Centre for Medium Range Weather Forecasts (ECMWF) with a 0.25° spatial resolution (http://data.ecmwf.int/data (accessed on 11 October 2022)). In this study, we selected daily 2 m dew point temperature, 2 m air temperature, surface net solar radiation, surface net thermal radiation, and surface solar radiation downwards from 2001 to 2018 as the meteorological data to drive the model, and the effect of altitude was also considered in the interpolation of temperature. All meteorological variables above were aggregated to 8-day time steps and resampled to 0.05° resolution using the bilinear interpolation method.

The MODIS land cover product MCD12C1 (https://e4ftl01.cr.usgs.gov/MOTA/MCD12C1.006/ (accessed on 11 October 2022)), from 2001 to 2018, was used to drive the model. Here, we selected the International Geosphere-Biosphere Programme (IGBP) classification product which consists of 17 land cover classifications with a spatial resolution of 0.05° and an annual interval.

To select vegetation indices that characterize canopy N concentrations for the ε_{max} estimation, we collected MODIS reflectance products MCD43A4 and MYDOCGA, which contain MODIS reflectance bands 1 to 7 and bands 8 to 16, respectively. The reflectance data were controlled by quality data, and the original time series vegetation indices were smoothed with the Savitzky-Golay (S-G) filtering method [57].

The SIF data were used to calculate the global T_{opt}^{eco}. Zhang et al. [58] generated a global continuous SIF (CSIF) dataset using satellite-retrieved SIF from the Orbiting Carbon Observatory-2 (OCO-2) and MODIS surface reflectance based on neural networks. We selected the all-sky daily average CSIF dataset at moderate spatiotemporal (0.05°, 4-day), which has strong spatiotemporal dynamics, to characterize the photosynthetic state of vegetation.

2.3. GPP Products Derived from Different Models

We collected multiple global GPP products, including four LUE GPP products, two data-driven GPP products, and two process model products, to compare with the GPP simulations in this study, as shown in Table 1. Among them, the FLUXCOM GPP, LPJ-GUESS GPP, and SDGVM GPP were resampled to 0.05° × 0.05° using a bilinear interpolation method.

Table 1. Multiple GPP products selected for comparison in this study.

Name	Model Type	Spatial Resolution	Temporal Resolution	References
MOD17 GPP	LUE model	0.05° × 0.05°	8 days	Zhao et al. [59]
rEC-LUE GPP		0.05° × 0.05°	8 days	Zheng et al. [26]
VPM GPP		0.05° × 0.05°	8 days	Zhang et al. [60]
MuSyQ GPP		0.05° × 0.05°	8 days	Wang et al. [19]
GOSIF GPP	Data-driven model	0.05° × 0.05°	8 days	Li and Xiao [61]
FLUXCOM GPP		0.083° × 0.083°	8 days	Jung et al. [62]
LPJ-GUESS GPP	Process-based model	0.5° × 0.5°	monthly	Smith et al. [63]
SDGVM GPP		0.5° × 0.5°	monthly	Walker et al. [64]

3. Methods

3.1. Calculation of the Optimum Temperature for Photosynthesis

We calculated the optimum temperature for photosynthesis at the site scale using in situ GPP and the global scale using satellite SIF data, respectively. Referring to Yang et al. [32], we first corresponded the long time series in situ GPP (or satellite SIF pixel values) to temperature to get the gray scatter plot in Figure 1. Then, these points were divided into multiple temperature bins at 1 °C intervals (as shown in Figure 1, the blue part was a temperature bin), and the 90% quantile of the in situ GPP (or satellite SIF pixel

value) in each bin was extracted as the response value at that temperature (as shown in Figure 1, the red point in the blue bin was the response value to this temperature). Finally, the response values in all the temperature bins were connected together to obtain the temperature response curve, and the highest value of the curve was set as the optimum temperature (Figure 1). The optimum temperature calculated by the in situ GPP was used to verify the global optimum temperature based on satellite SIF data.

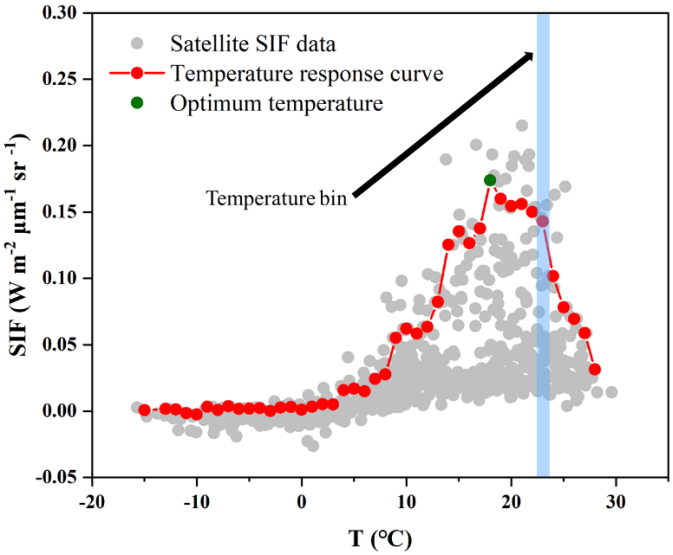

Figure 1. Optimum temperature calculation based on a satellite SIF pixel.

3.2. Product Algorithm

The NI-LUE model is based on the LUE model considering temperature and water, and further integrates the effect of CO_2 fertilization, radiation components and canopy N concentrations. The schematic workflow of the NI-LUE model was shown in Figure 2 and GPP can be estimated as follows:

$$GPP = (p \times [NI] + q) \times f(T) \times f(W) \times f(CO_2) \times [f(PAR_{su}) \times APAR_{su} + f(PAR_{sh}) \times APAR_{sh}] \quad (2)$$

where p and q are parameters optimized for different vegetation types; $[NI]$ represents the vegetation index selected to characterize the canopy N concentrations. This study collected the vegetation indices used in previous studies to estimate canopy N (Table A1). These indices were used separately to drive the model and to obtain the optimal vegetation index that would result in the best model performance.

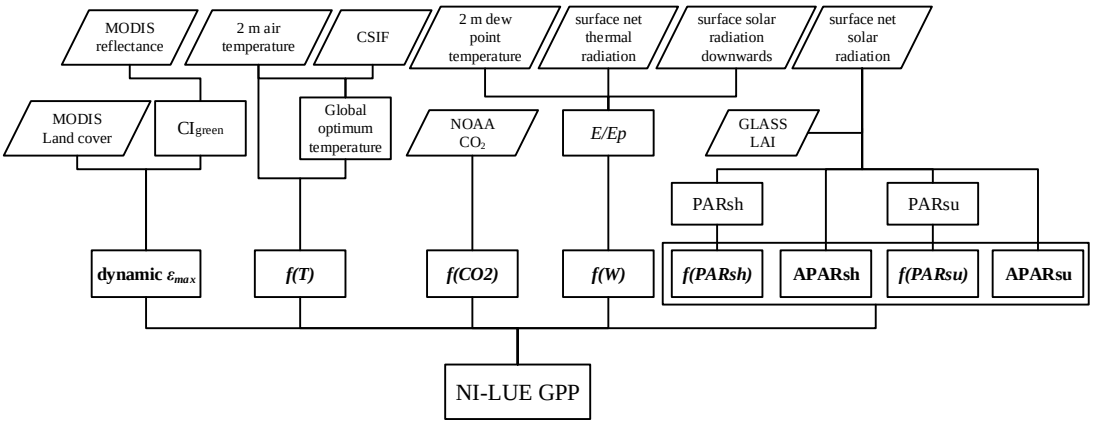

Figure 2. Datasets and workflow of NI-LUE model to calculate GPP.

$f(T)$ and $f(W)$ are the scalars of temperature and water, respectively. $f(T)$ was calculated according to the Terrestrial Ecosystem Model (TEM) as the following formula [26]:

$$f(T) = \frac{(T_a - T_{min})(T_a - T_{max})}{(T_a - T_{min})(T_a - T_{max}) - (T_a - T_{opt})^2} \quad (3)$$

where T_a represents the air temperature (°C). T_{opt}, T_{min} and T_{max} are the optimum, minimum, and maximum air temperature for vegetation growth, respectively. In this model, T_{opt} was the global T_{opt}^{eco} calculated in Section 3.1. T_{min} and T_{max} were set as shown in Table 2. For $f(W)$, we described it using the actual evapotranspiration (E) and the potential evapotranspiration (E_p) as follows:

$$f(W) = 0.5 + 0.5\left(\frac{E}{E_p}\right) \quad (4)$$

where E was calculated based on the revised Penman-Monteith model. Since the Penman-Monteith model requires the canopy resistance of different vegetation types under sufficient water conditions [65,66], we used the Priestley-Taylor equation for E_p calculations [67–71]. The detailed calculation method can be found in Cui et al. [67].

The effect of CO_2 fertilization ($f(CO_2)$) was integrated into our model with reference to the revised EC-LUE model [26] as follows:

$$f(CO_2) = \frac{C_i - \varphi}{C_i + 2\varphi} \quad (5)$$

$$C_i = [CO_2] \times \chi \quad (6)$$

where φ is the CO_2 compensation point in the absence of dark respiration, which was set for different vegetation types according to Zheng et al. [26] as shown in Table 2; C_i indicates the internal leaf CO_2 concentrations and was calculated using the product of the atmospheric CO_2 concentrations ($[CO_2]$) and χ, which represents the ratio of the C_i and $[CO_2]$ which can be calculated as follows:

$$\chi = \frac{\xi}{\xi + \sqrt{VPD}} \quad (7)$$

$$VPD = SVP \times (1 - RH) \quad (8)$$

$$SVP = 0.6112 \times e^{\frac{17.67 \times T_a}{T_a + 243.5}} \quad (9)$$

$$RH = e^{\frac{17.625 \times DT}{DT + 243.04} - \frac{17.625 \times T_a}{T_a + 243.04}} \quad (10)$$

$$\xi = \sqrt{\frac{356.51K}{1.6\eta^*}} \quad (11)$$

where parameter ξ represents the sensitivity of VPD to χ; K is the Michaelis-Menten coefficient of Rubisco; η^* is the viscosity of water relative to its value at 25 °C.

$$K = K_c\left(1 + \frac{P_o}{K_o}\right) \quad (12)$$

$$K_c = 39.97 \times e^{\frac{79.43 \times (T_K - 298.15)}{298.15 \times R \times T_K}} \quad (13)$$

$$K_o = 27480 \times e^{\frac{36.38 \times (T_K - 298.15)}{298.15 \times R \times T_K}} \quad (14)$$

where P_o is the partial pressure of O_2, approximated as 21,278.25 Pa; K_c and K_o are the Michaelis-Menten constants of CO_2 and O_2, respectively; T_K is the air temperature with unit K; and R is the molar gas constant and is set to 8.314 J/mol/K.

We further considered the effect of radiation components. Since the differences between the LUE of sunlit and shaded leaves are mainly influenced by light intensity, their ε_{max} should be similar [3,72]. Considering the hyperbolic relationship between PAR and LUE, we used the PAR of the shaded (PAR_{sh}) and sunlit leaves (PAR_{su}) to calculate the radiation constraints, and we decomposed the APAR into APAR of the shaded ($APAR_{sh}$) and sunlit leaves ($APAR_{su}$). $f\ (PAR_{su})$ and $f\ (PAR_{sh})$ are the radiation scalars for sunlit and shaded leaves, respectively, calculated as Equations (15) and (16).

$$f(PAR_{su}) = \frac{1}{a \times PAR_{su} + 1} \tag{15}$$

$$f(PAR_{sh}) = \frac{1}{a \times PAR_{sh} + 1} \tag{16}$$

where a is optimized according to different vegetation types.

PAR_{su}, PAR_{sh}, $APAR_{su}$, and $APAR_{sh}$ can be calculated based on the BEPS model [38] as follows:

$$PAR_{sh} = \frac{PAR_{dif} - PAR_{dif,u}}{LAI} + C \tag{17}$$

$$PAR_{su} = \frac{PAR_{dir} \times \cos(\beta)}{\cos(\theta)} + PAR_{sh} \tag{18}$$

$$PAR_{dif,u} = PAR_{dif} \times e^{\left(-0.5 \times \Omega \times \frac{LAI}{\cos(\overline{\theta})}\right)} \tag{19}$$

$$\cos(\overline{\theta}) = 0.537 - 0.025 \times LAI \tag{20}$$

$$C = 0.07 \times \Omega \times PAR_{dir} \times (1.1 - 0.1 \times LAI) \times e^{(-\cos(\theta))} \tag{21}$$

$$APAR_{su} = (1 - \alpha) \times PAR_{su} \times LAI_{su} \tag{22}$$

$$APAR_{sh} = (1 - \alpha) \times PAR_{sh} \times LAI_{sh} \tag{23}$$

where PAR_{dif} and PAR_{dir} are the diffuse and direct PAR, respectively; $PAR(\mathrm{MJ/m^2})$ was calculated using 0.48 times the surface solar radiation downwards from ERA-5; the PAR_{dif} was calculated by parameter calibration using the clear sky index [38,73]; PAR_{dir} is the residual of PAR minus PAR_{dif}; C is the multiple scattering effects of direct radiation; β is set to 60° indicating the mean leaf-sun angle; θ is the solar zenith angle; $\overline{\theta}$ is a representative zenith angle for diffuse radiation transmission; Ω and α are the clumping index and the canopy albedo, which were set for different vegetation types according to Tang et al. [74] and Zhang et al. [75], respectively (Table 2); LAI_{su} and LAI_{sh} denote the LAI of sunlit and shaded leaves, respectively, and were calculated as follows:

$$LAI_{su} = 2 \times \cos(\theta) \times \left(1 - e^{\left(-0.5 \times \Omega \times \frac{LAI}{\cos(\theta)}\right)}\right) \tag{24}$$

$$LAI_{sh} = LAI - LAI_{su} \tag{25}$$

3.3. Model Parameterization and Validation

The Shuffled Complex Evolution Procedure Developed at the University of Arizona (SCE-UA) is a global optimization algorithm which aims to find the optimal values of parameters in a particular range which makes sure that the cost function is minimized [76]. The expression of the cost function is as follows:

$$d = 1 - \frac{RMSE^2}{\sum_{i=1}^{n}(x_i - \overline{x})^2 + \sum_{i=1}^{n}(y_i - \overline{x})^2 + 2 \times \left| \frac{\sum_{i=1}^{n}(x_i - \overline{x})(y_i - \overline{y})}{\sqrt{\sum_{i=1}^{n}(x_i - \overline{x})^2 \ \sum_{i=1}^{n}(y_i - \overline{y})^2}} \times \sqrt{\sum_{i=1}^{n}(x_i - \overline{x})^2} \times \sqrt{\sum_{i=1}^{n}(y_i - \overline{x})^2} \right|} \tag{26}$$

where the *RMSE* is the root-mean-square error; n is the total number of data used for model parameters' optimization; x_i and y_i represent in situ GPP and estimated GPP from the model, respectively; $\overline{x}$ and $\overline{y}$ are the mean values of in situ GPP and estimated GPP. In this study, p, q, and a in Equations (2), (15), and (16) were optimized using the SCE-UA algorithm. To ensure the robustness of the model, we used a 10-fold cross-validation method to optimize the parameters and validate the model. First, we randomly divided the in situ GPP of each vegetation type into 10 groups, using 9 groups of data to train and optimize the parameters and one group of data for validation, ensuring that all data were involved in training and validating the model. Then, we trained 10 models and obtained 10 sets of parameters, and the average of the these parameters was used for the generation of global GPP products. Finally, the standard deviation of the global GPP generated by the ten sets of parameters was used as the uncertainty of the product.

Table 2. Parameters T_{max}, T_{min}, clumping index (Ω), and albedo(α) of different vegetation types. The vegetation types include cropland (CRO), closed shrubland (CSH), deciduous broadleaf forest (DBF), deciduous needleleaf forest (DNF), evergreen broadleaf forest (EBF), evergreen needleleaf forest (ENF), grassland (GRA), mixed forest (MF), open shrubland (OSH), savanna (SAV), permanent wetland (WET), and woody savanna (WSAV).

IGBP	CRO	CSH	DBF	DNF	EBF	ENF	GRA	MF	OSH	SAV	WET	WSA
T_{max}	48	48	40	40	48	40	48	48	48	48	40	48
T_{min}	−1	−3	−1	−1	2.5	−1	1	−2	−3	−1	0	−1
φ [a]	45	34	32	32	20	25	57	49	34	54	36	54
Ω [b]	0.9	0.8	0.8	0.6	0.8	0.6	0.9	0.7	0.8	0.8	0.9	0.8
α [c]	0.153	0.132	0.134	0.112	0.137	0.102	0.182	0.122	0.185	0.153	0.105	0.134

[a] Zheng et al. [26]; [b] Tang et al. [74]; [c] Zhang et al. [75].

The coefficient of determination (R^2), the RMSE, and the mean absolute error (MAE) were used to evaluate the performace of the GPP estimation. Furthermore, the index of agreement (IOA), which measures the degree of agreement between the estimates and observations, was selected [77]. The logical range of IOA is 0 to 1, where 1 indicates that the model estimates are consistent with the observations, and 0 represents complete disagreement.

3.4. Evaluation of Spatial Performance

To demonstrate the rationality of the spatial distribution of GPP products, we compared the spatial distribution of our product with other GPP products. In this study, the SPAtial Efficiency (SPAEF) was used as a metric to evaluate the consistency of two spatial pattern maps. SPAEF is a bias-insensitive spatial performance metric, which improved the structure of the Kling-Gupta efficiency [78].

$$\mathrm{SPAEF} = 1 - \sqrt{(r-1)^2 + (\beta-1)^2 + (\gamma-1)^2} \quad (27)$$

where r is the Pearson correlation coefficient between the two spatial pattern maps, β is the ratio of the coefficient of variations (CV) of the two spatial pattern maps, and γ is the percentage of histogram intersections of the two spatial pattern maps after normalization to a mean of 0 and standard deviation of 1 (z score).

3.5. Contribution of Each Variable to Long-Term Variations in GPP

To assess the contributions of multiple variables to GPP simulation, including the meteorological variables, CO_2 concentrations, LAI, land use cover, and nitrogen index, we constructed two types of simulation experiments using our LUE model. The first experiment (S_{ALL}) was that the model was running normally, and each variable varied over time. The second experiment (S_{i0}) was to fix one variable (i) in the initial state, and other variables varied with time. Meteorological variables, atmospheric CO_2 concentrations,

LAI, land cover, and N index were used as fixed variables in the second experiment, respectively, and the interannual changes of GPP simulation (NI-LUE$_{i0}$) were obtained under the assumption that each variable was unchanged. The total of the differences in the GPP simulations of S_{ALL} and S_{i0} for each year from 2001 to 2018 ($\sum$NI-LUE-NI-LUE $_{i0}$) was the contribution of variable *i* to the long-term changes in GPP.

4. Results

4.1. Distribution of Global Ecosystem-Scale Optimum Temperature for Photosynthesis

The distribution of global T_{opt}^{eco} based on long-term CSIF was shown in Figure 3a. In general, the average T_{opt}^{eco} over the vegetated areas was 20.17 ± 5.57 °C and T_{opt}^{eco} varied from 15∼30 °C in approximately 82.47% of the vegetated area. The global T_{opt}^{eco} presented a decreasing trend from low latitudes to high latitudes, except that the average T_{opt}^{eco} in the vegetated area of the Qinghai-Tibet Plateau was 10.58 ± 3.55 °C, showing a significant spatial gradient. In this study, T_{opt}^{eco} calculated by the in situ GPP was used to verify the global T_{opt}^{eco} based on satellite SIF, and the relationship between them was shown in Figure 3b. Satellite SIF-derived T_{opt}^{eco} was comparable to that calculated by in situ GPP (R^2 = 0.63, RMSE = 3.15 °C), which provided support for estimating global T_{opt}^{eco} using CSIF data. Among all vegetation types, EBF, CRO, DBF, SAV, and WSA had higher T_{opt}^{eco}, while the mean T_{opt}^{eco} of ENF, DNF, and GRA were lower (Figure 3c). When we calculated the global GPP, if there were too many invalid data and the temperature response curve was not statistically significant, we used the average optimal temperature of the vegetation type in Figure 3c to replace the optimal temperature of this pixel.

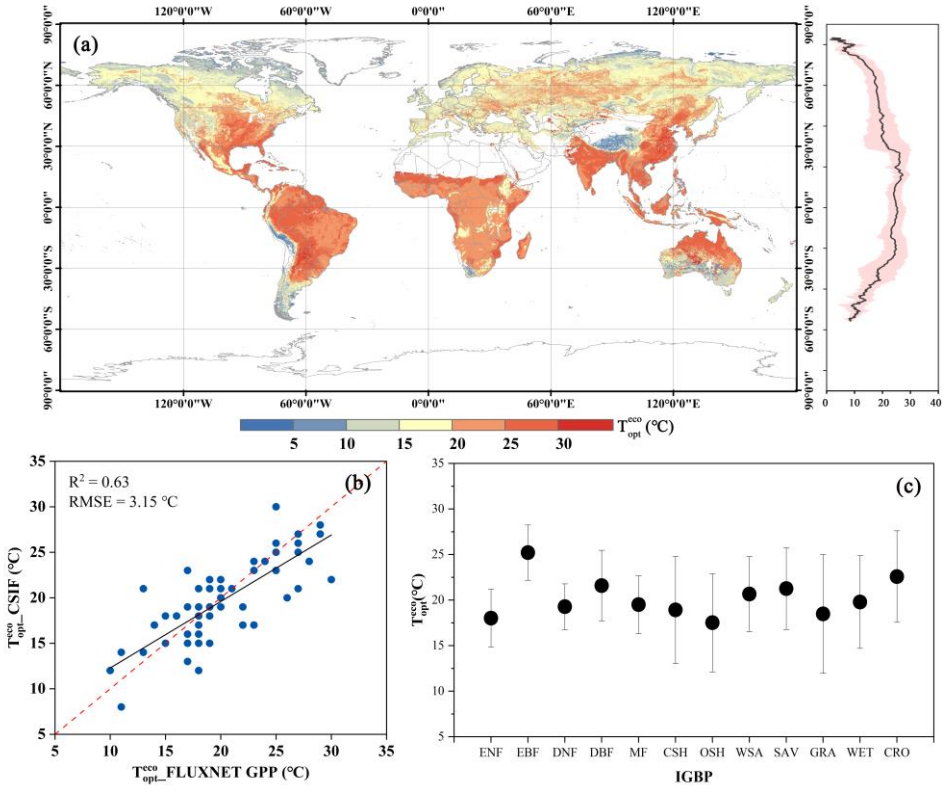

Figure 3. (**a**) Global ecosystem-scale optimum temperature for photosynthesis (T_{opt}^{eco}); (**b**) Relationship between in situ GPP and satellite SIF-derived T_{opt}^{eco}; (**c**) T_{opt}^{eco} for different vegetation types. The vegetation types include evergreen needleleaf forest (ENF), evergreen broadleaf forest (EBF), deciduous needleleaf forest (DNF), deciduous broadleaf forest (DBF), mixed forest (MF), closed shrubland (CSH), open shrubland (OSH), woody savanna (WSAV), savanna (SAV), grassland (GRA), permanent wetland (WET), and cropland (CRO).

4.2. Canopy N Concentrations Index Selection and Model Parameter Optimization

Vegetation indices that have previously been used to estimate canopy N content were used to drive the model. The performance of each index was evaluated by comparing the accuracy of GPP estimated by the models driven by in situ meteorological data and these indices (Figure 4). Among all vegetation indices, the GPP simulation using CI_{green} performed the best, followed by the chlorophyll/carotenoid index (CCI), the green normalized difference vegetation index (GNDVI) and the near-infrared reflectance (NIR).

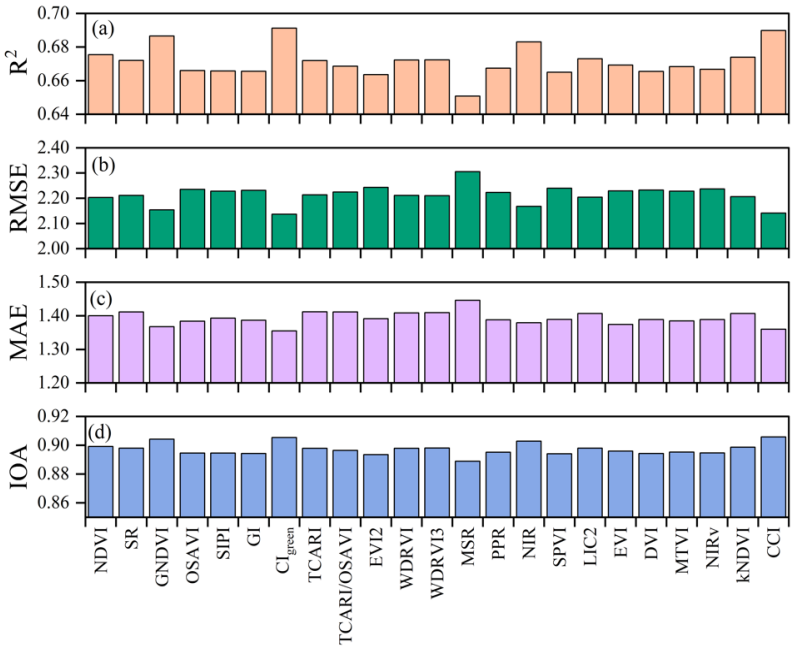

Figure 4. (**a**) The coefficient of determination (R^2), (**b**) the root-mean-square error (RMSE) ($gC/m^2/d$), (**c**) the mean absolute error (MAE) ($gC/m^2/d$), and (**d**) the index of agreement (IOA) of GPP simulations based on different vegetation indices.

Moreover, we collected some measured canopy N concentrations data to demonstrate the correlation between CI_{green} and canopy N concentrations. As shown in Figure 5, there was a strong correlation between CI_{green} and canopy N concentrations (r = 0.82). Similarly, many studies also suggested that CI_{green} can be used to quantify canopy N concentrations. For example, He et al. [52] found that the R^2 between the canopy N concentrations of winter wheat and CI_{green} at different viewing zenith angles reached 0.6~0.75; Mutowo et al. [79] predicted the woodland leaf N concentrations using random forests and found that CI_{green} had the highest importance among multiple vegetation indices; Clevers and Gitelson [80] found that CI_{green} and canopy N of grass and potato were linearly correlated (R^2 of 0.77 and 0.89, respectively). Therefore, we selected CI_{green} as the nitrogen index (NI) in this study to characterize the canopy N concentrations and introduced it into the LUE model to calculate the ε_{max}.

As shown in Figure 6, we verified the accuracy of the GPP simulation using CI_{green} and the ERA5 meteorological data based on the 10-fold cross-validation. The model overall has a high estimation accuracy (R^2 = 0.63 ± 0.01, RMSE = 2.27 ± 0.05 $gC/m^{2/}d$, MAE = 1.48 ± 0.03 $gC/m^2/d$, IOA = 0.88 ± 0.01). Parameters optimized according to different vegetation types were shown in Table A3. Among all vegetation types, the GPP estimates of DBF had the highest accuracy, followed by GRA, WSA, and WET. The GPP estimation accuracy of CRO, EBF, and MF was relatively poor, with R^2 below 0.5.

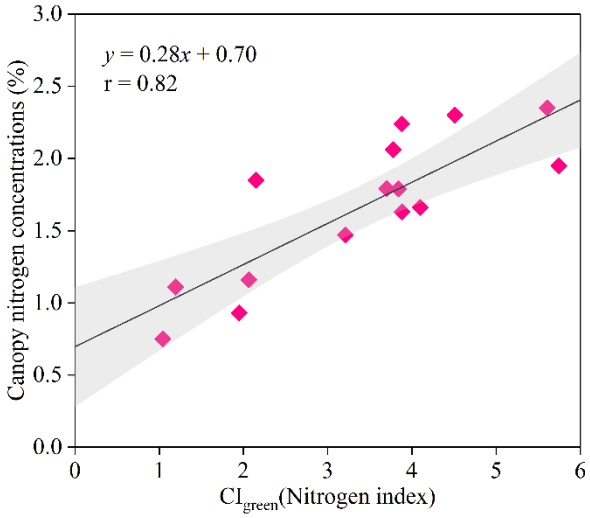

Figure 5. Relationship between CI_{green} and canopy N concentrations (%). The grey area indicates the 95% confidence interval.

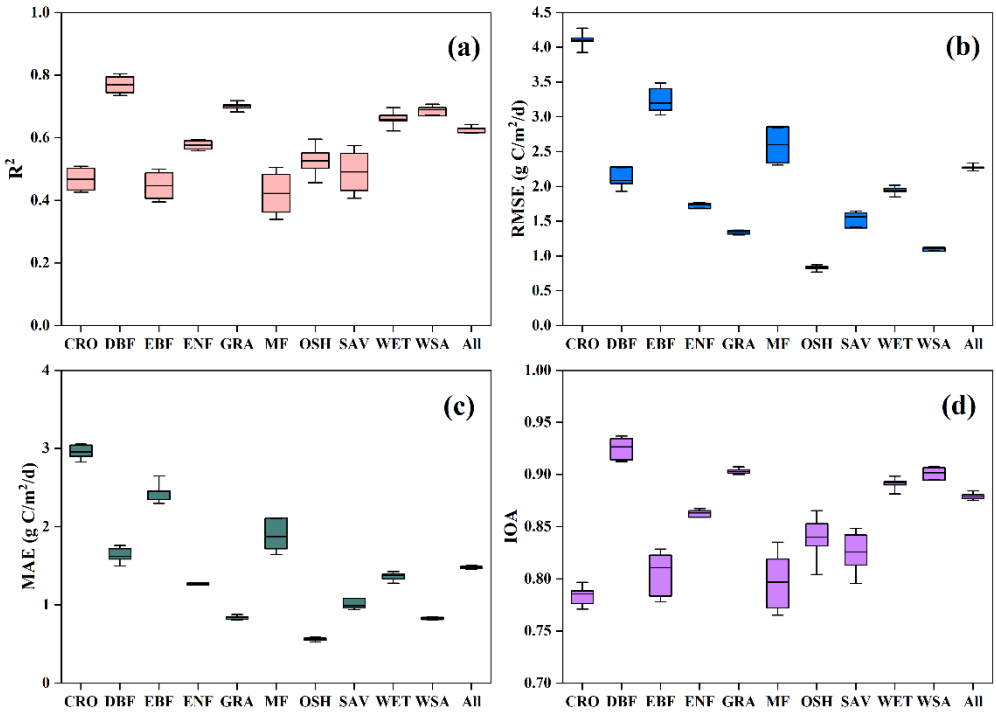

Figure 6. 10-fold cross validation of the model driven by ERA5 meteorological data for different vegetation types, using (**a**) the coefficient of determination (R^2), (**b**) the root-mean-square error (RMSE) ($gC/m^2/d$), (**c**) the mean absolute error (MAE) ($gC/m^2/d$), and (**d**) the index of agreement (IOA) as the accuracy evaluation indices. The vegetation types include cropland (CRO), closed shrubland (CSH), deciduous broadleaf forest (DBF), deciduous needleleaf forest (DNF), evergreen broadleaf forest (EBF), evergreen needleleaf forest (ENF), grassland (GRA), mixed forest (MF), open shrubland (OSH), savanna (SAV), permanent wetland (WET), and woody savanna (WSAV).

4.3. Spatiotemporal Patterns in Global GPP

A global GPP product was produced based on an improved LUE model that simultaneously considered multiple environmental factors and the canopy N concentrations index. The global mean annual GPP, from 2001 to 2018, was 129.7 ± 3.02 PgC. The spatial pattern of global annual GPP was shown in Figure 7. The GPP was high in tropical regions where sufficient water and suitable temperature can satisfy the photosynthesis of vegetation.

While the GPP gradually decreased with increasing latitude, cold or arid environmental conditions limited the growth of vegetation.

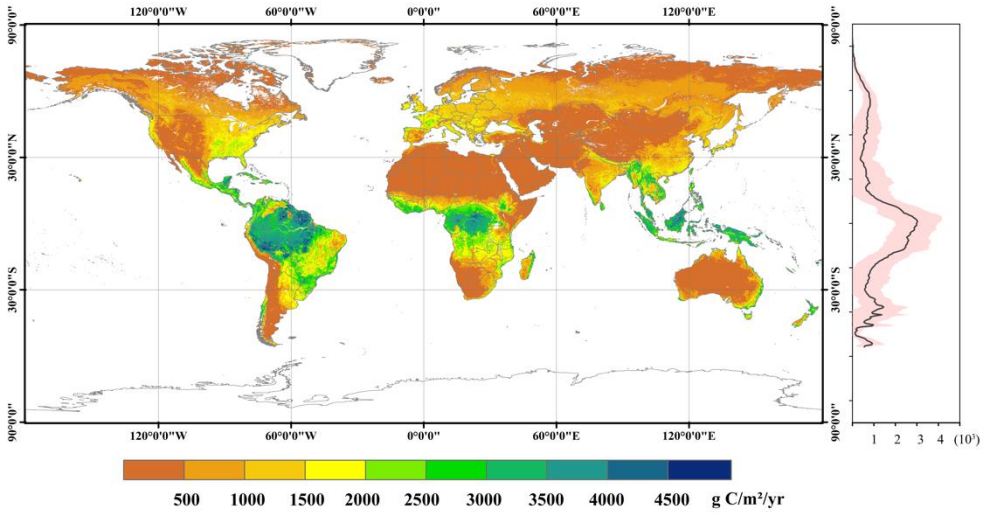

Figure 7. Spatial pattern of global GPP estimated by the NI-LUE model during 2001–2018.

Figure 8 showed the interannual variation trend of global GPP estimated by the NI-LUE model from 2001 to 2018. In the past 18 years, GPP showed an increased trend in about 60.1% of terrestrial ecosystems. In addition, the GPP in Central Africa, Central South America, Western Europe, Eastern China, and western India showed a rapidly increasing trend. However, there was a significant decreasing trend in eastern South America and tropical Southeast Asia. In high latitudes, GPP varied less and showed an increasing trend.

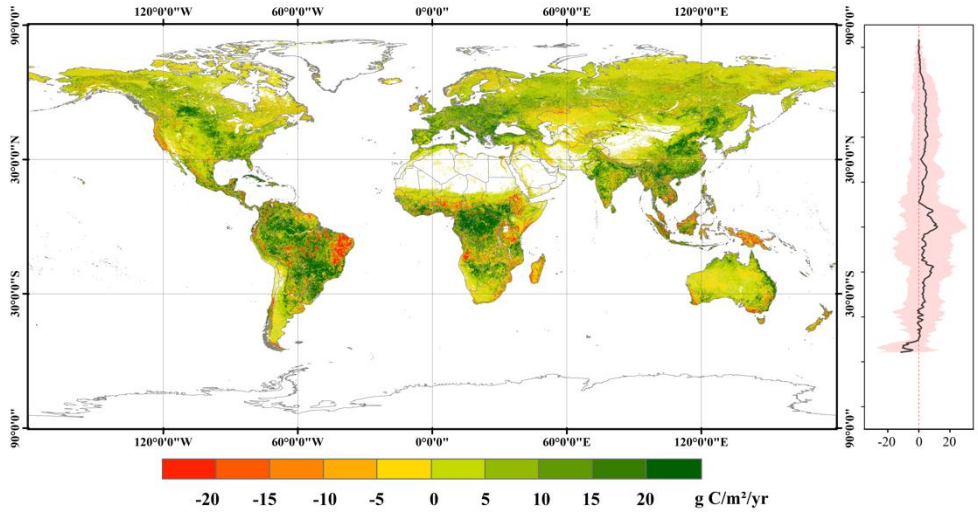

Figure 8. Spatial pattern of interannual variation trend of global GPP estimated by the NI-LUE model from 2001 to 2018.

Additionally, we used 10 sets of parameters obtained by a 10-fold cross-validation to simulate the global GPP separately to determine the uncertainty of the model. Globally, the mean uncertainty of the annual GPP simulation was 15.86 $gC/m^2/yr$. The spatial pattern of the uncertainty in the global GPP simulation (Figure 9) showed that GPP uncertainty was low at middle and high latitudes, while GPP uncertainty was high in eastern South America and central Africa.

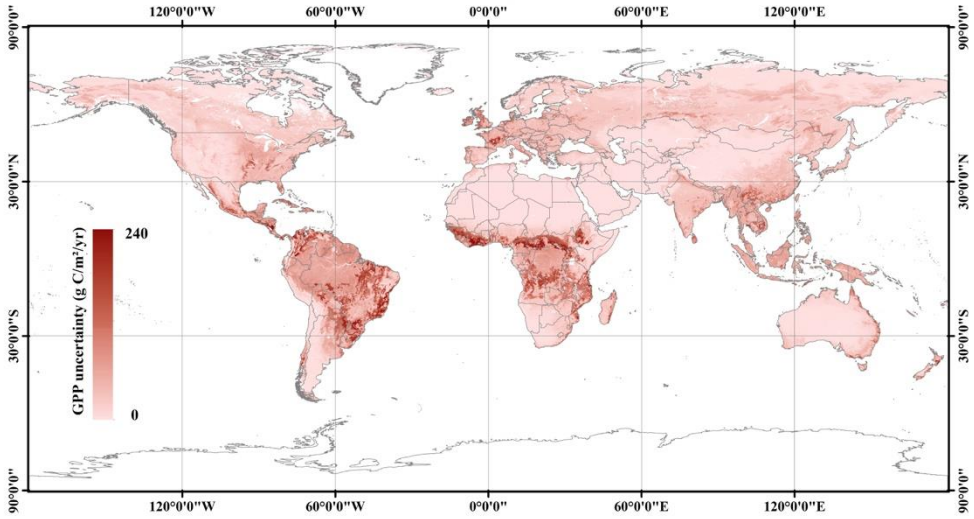

Figure 9. Spatial pattern of the uncertainty in global GPP estimated by the NI-LUE model.

4.4. Comparison with Other Global GPP Products

In this study, we used FLUXNET GPP data accumulated over three years to evaluate the daily and yearly simulation accuracy of different global GPP products. Figure 10 showed comparisons between FLUXNET GPP and various GPP products at 8-day time scales. Among all products, the NI-LUE GPP generated in this study had a good performance (R^2 = 0.65, RMSE = 2.43 $gC/m^2/d$, MAE = 1.73 $gC/m^2/d$, IOA = 0.89). MuSyQ, VPM, GOSIF, and FLUXCOM GPP products also have high accuracy, with R^2 exceeding 0.6. FLUXCOM GPP had the highest R^2 of all products, reaching 0.67. The MOD17 GPP product performed the worst, with an R^2 of only 0.55 and a significant underestimation. It was worth noting that, compared with other products, the linearly fitted line of NI-LUE GPP was closer to the 1:1 line, and the underestimation phenomenon was significantly weakened (slope = 0.72). Figure 11 further showed the comparison of simulation accuracy of various GPP products for different vegetation types. Compared with different GPP products, the performances of NI-GPP improved in GPP simulations of CRO, DBF, EBF, and GRA. For SAV, WET, and WSA, although GOSIF GPP performed the best among all products, NI-LUE still had an advantage in all products based on LUE models. For ENF, MF, and OSH, the performance of NI-GPP was not outstanding, while MuSyQ GPP, FLUXCOM GPP, and GOSIF GPP performed better for these vegetation types, respectively.

Moreover, the annual GPP simulations of two process-based biophysical models in TRENDY, LPJ-GUESS, and SDGVM, were added to the comparison. As shown in Figure 12, the annual GPP simulations of LPJ-GUESS and SDGVM had poor performance, showing significant underestimation. Compared to the verification of daily GPP estimates, the accuracy of other products improved. Among them, the NI-LUE GPP produced in this study still had a good performance in the annual GPP verification, and the annual GPP of rEC-LUE, MuSyQ, GOSIF, and FLUXCOM also performed well, with an R^2 exceeding 0.7. Across all products, the regression line between the annual gross GPP of NI-LUE, MuSyQ, and GOSIF and FLUXNET GPP is closer to the 1:1 line, with a slope exceeding 0.75.

Figure 13a showed the inter-annual variations in the annual total GPP of different products. There were great differences in the global annual total GPP of different products, ranging from 104.48 Pg C to 137.28 Pg C. Among all products, the global annual total GPP of the five LUE models ranged from 108.79 Pg C to 129.70 Pg C. The annual total GPP simulations of two process-based biophysical models in TRENDY differed considerably, with LPJ-GUESS GPP of 106.62 Pg C and SDGVM GPP of 133.65 Pg C. However, these two products had similar trends, and they can reflect the fluctuations around 2009 as well as the NI-LUE GPP produced in this study. For data-driven GPP products, the global annual total GPP of GOSIF GPP was the highest (137.28 Pg C), while that of FLUXCOM GPP was

the lowest (104.48 Pg C). The global annual total NI-LUE GPP ranged from 125.09 Pg C to 133.75 Pg C from 2001 to 2018, placing at the middle of the various GPP products, which is in a reasonable range based on statistics for other products. Figure 13b showed the correlation coefficient matrix of the interannual variations of different products. The study showed that the interannual variation of NI-LUE GPP was significantly positively correlated with GOSIF GPP, FLUXCOM GPP, VPM GPP, LPJ-GUESS GPP, and SDGVM GPP, and the correlation coefficients with MOD17 GPP and MuSyQ GPP were only 0.36 and 0.33, respectively. However, since rEC-LUE GPP showed a decreasing trend from 2001 to 2018, it was negatively correlated with most of the GPP products.

To demonstrate that the spatial pattern of NI-LUE GPP products was reasonable, we separately calculated the SPAEF between the mean annual NI-LUE GPP and different GPP products. Figure 14 showed that the SPAEF of NI-LUE GPP and other products were all above 0.5, and the spatial consistency with rEC-LUE and MuSyQ was the highest, with an SPAEF of 0.86 and 0.83, respectively. Due to the lower spatial resolution of LPJ-GUESS and SDGVM, the spatial consistency with NI-LUE GPP was relatively poor, with an SPAEF of 0.51 and 0.55, respectively.

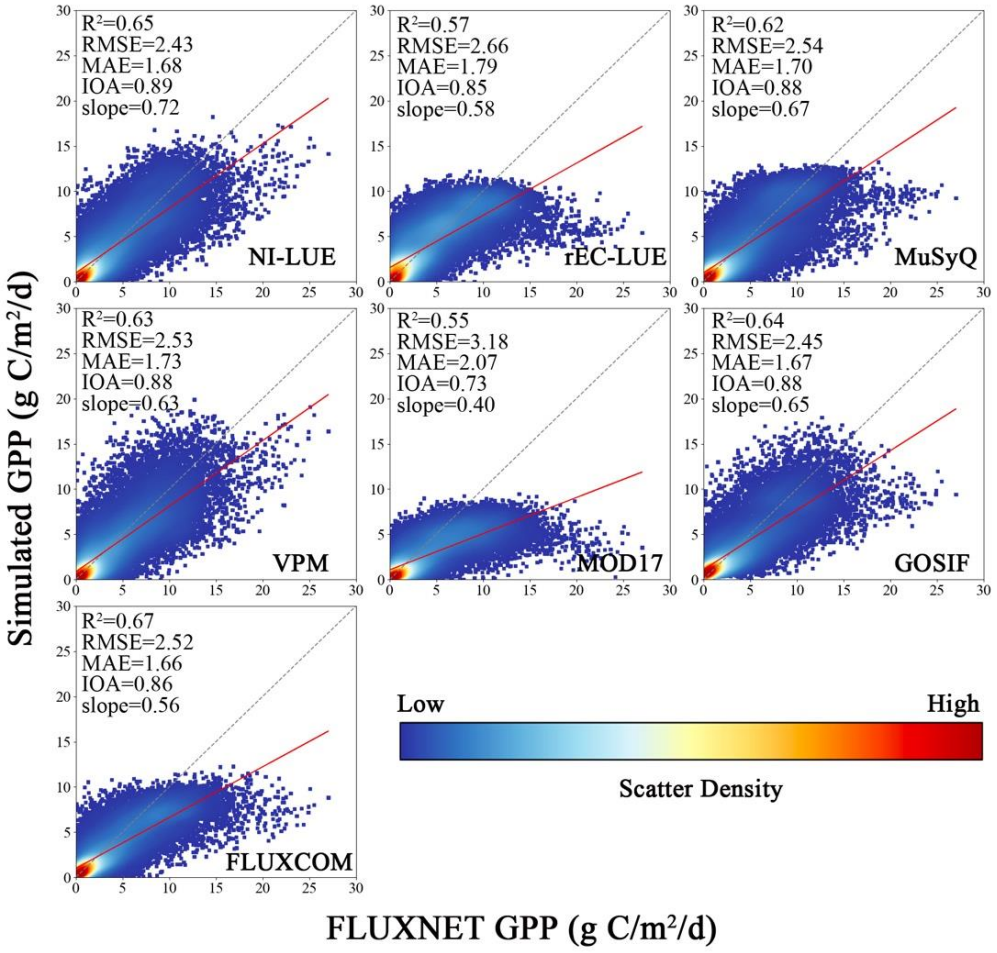

Figure 10. Comparisons between FLUXNET GPP and various GPP products at 8-day time scales. Dashed lines are 1:1 lines. Red solid lines are linearly-fitted lines.

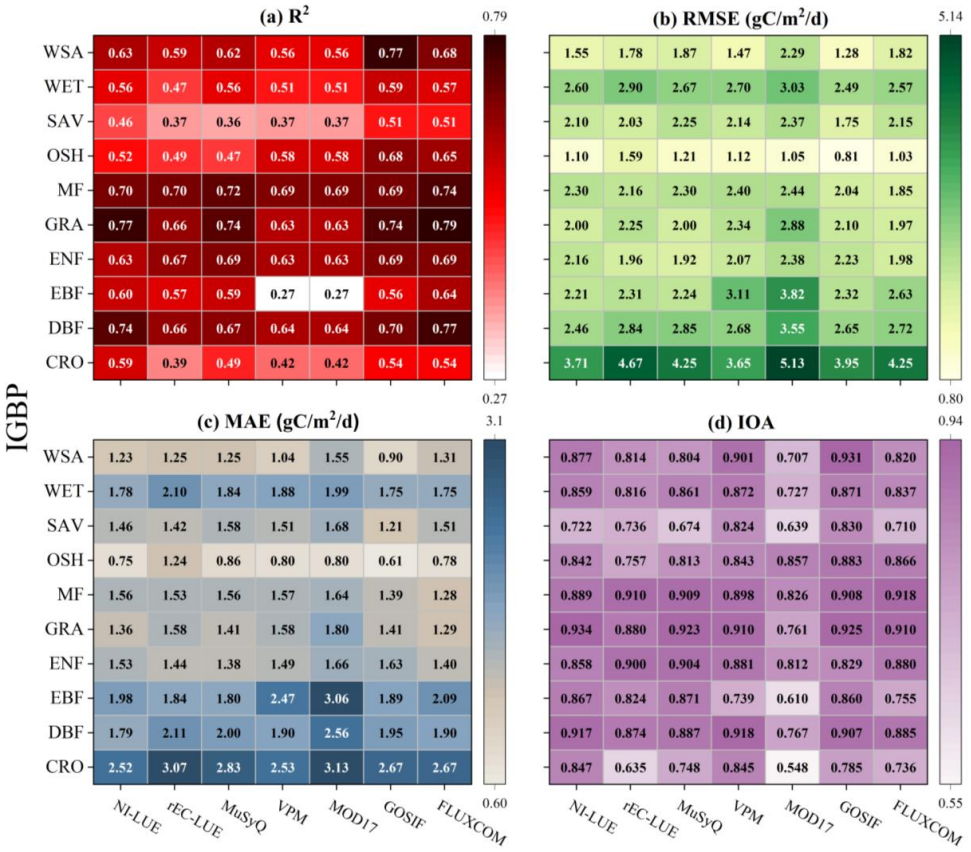

Figure 11. Comparison of simulation accuracy of various GPP products for different vegetation types at 8-day time scales.

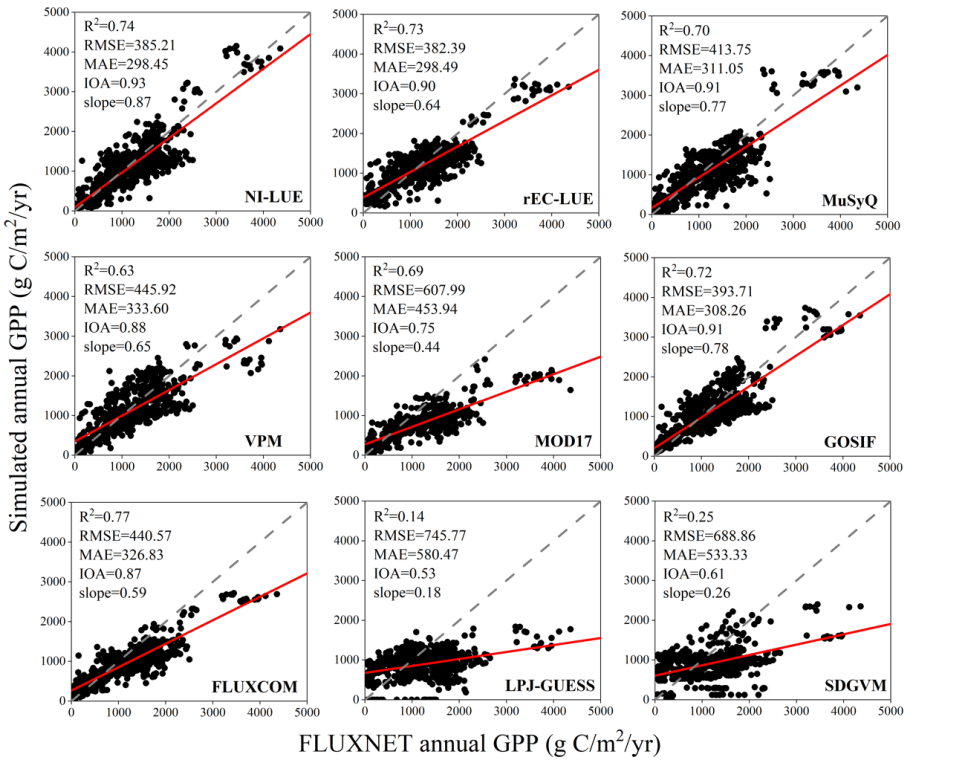

Figure 12. Comparisons between FLUXNET GPP and various GPP products at yearly time scales. Dashed lines are 1:1 lines. Red solid lines are linearly fitted lines.

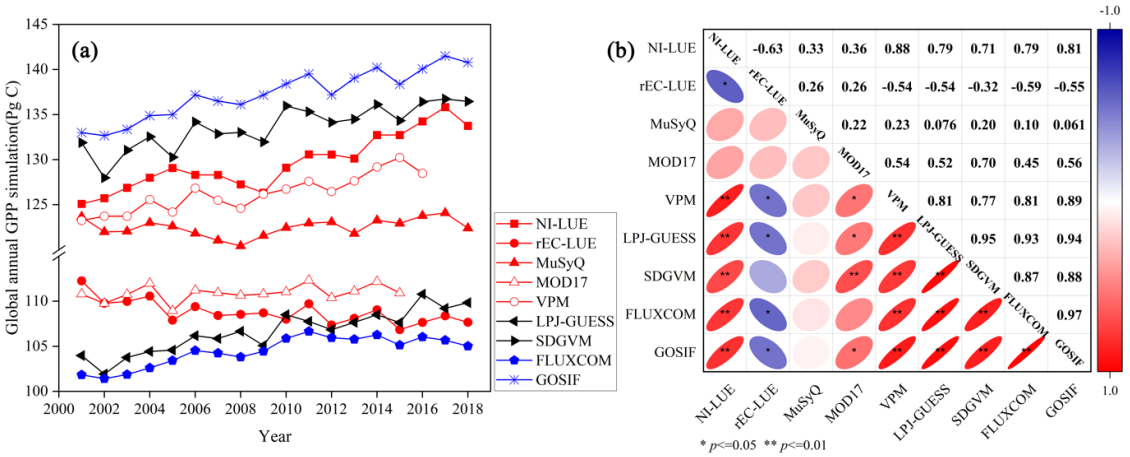

Figure 13. (**a**) Comparisons of global annual total GPP from different products; (**b**) correlation coefficient matrix of inter-annual variations of total GPP of different products.

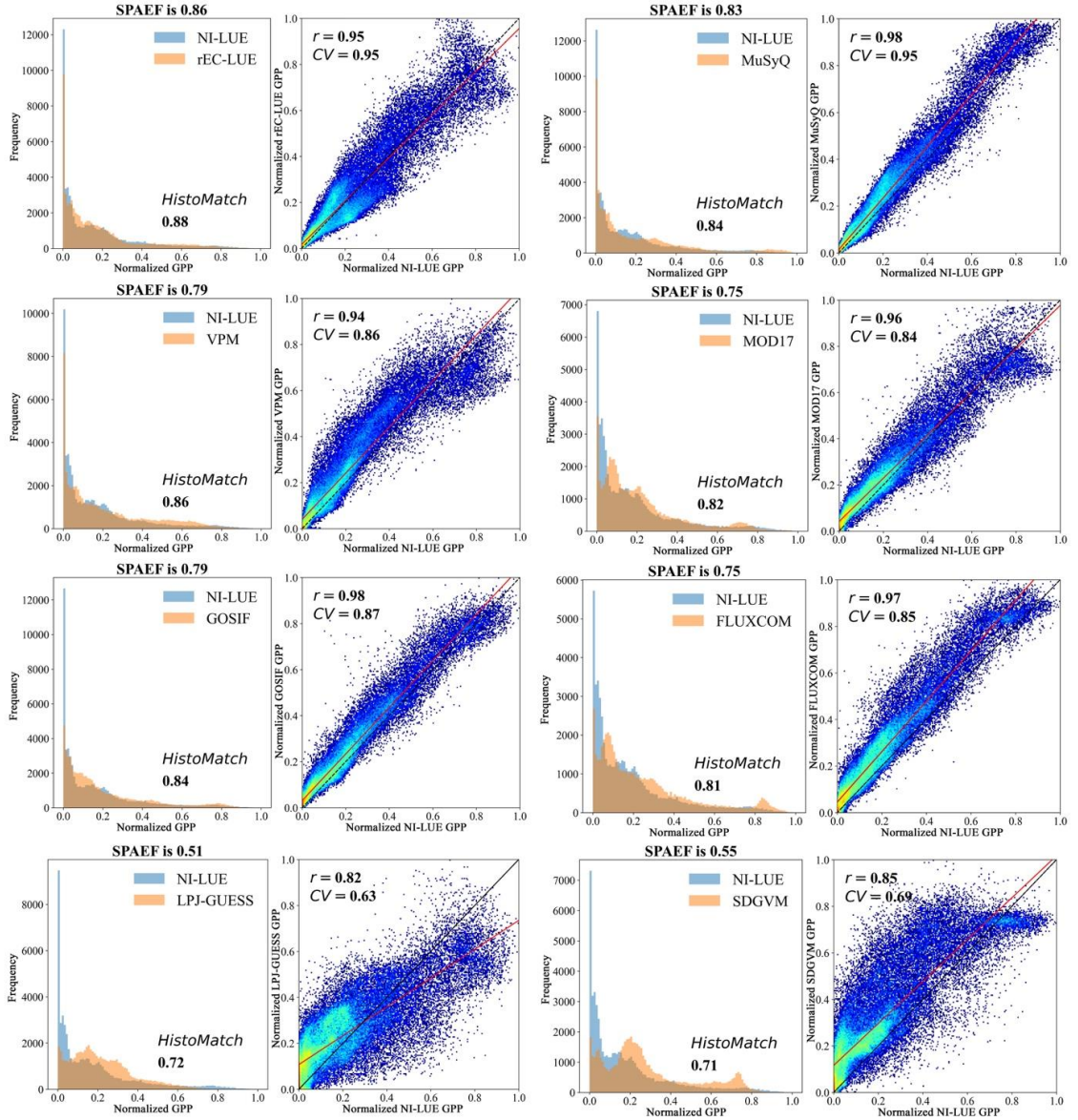

Figure 14. SPAtial Efficiency (SPAEF) between NI-LUE GPP and different GPP products.

5. Discussion

5.1. Contributions of Multiple Variables to the GPP Simulation

To quantify the contribution of climate variables (including temperature, radiation, and dew point temperature), atmospheric CO_2 concentrations, LAI, land cover, and vegetation indices that characterize canopy N concentrations to changes in global annual total GPP from 2001 to 2018, we fixed variable *i* (*i* = climate variables, CO_2 concentrations, LAI, Land cover, NI) at the initial state to simulate the interannual variation of global GPP (Figure 15). Moreover, Figure 16 showed the spatial patterns of cumulative contributions of various variables to global annual GPP from 2001 to 2018. Under the normal situation (S_{All}), each variable changes normally over time, and the global annual GPP simulation (NI-LUE) increased at a rate of 0.53 Pg C/yr from 2001 to 2018. In contrast, the global GPP simulation (NI-LUE_{i0}) under other situations showed different trends.

With the climate variables fixed at the initial state (2001), the global annual GPP simulation (NI-LUE_{Cli0}) increased at a rate of 0.52 Pg C/yr from 2001 to 2018. Among all variables, climate variables may be more of a moderator. In 2009, for example, El Niño led to higher surface temperatures, and warmer and drier climate conditions [81]. The NI-LUE GPP under the normal situation dropped suddenly in 2009, consistent with the GPP trends simulated by the two process-based biophysical models in Figure 13a, while the NI-LUE_{Cli0} kept rising during the year. From 2001 to 2018, the cumulative contribution of climate variables to global GPP simulation was 12.39 Pg C. As shown in Figure 16a, the positive contributions of climate variables were mainly distributed in northern and southern South America, western North America, western Europe, central Africa, and southern China, while in eastern North America and the northern coast of South America regions, as well as the island of New Guinea in Southeast Asia, the contribution of climate variables was negative, reducing GPP in these regions.

Atmospheric CO_2 concentrations significantly accelerated global GPP increase. The global annual GPP simulation (NI-LUE_{CO20}) increased at a rate of 0.33 Pg C/yr with the atmospheric CO_2 concentrations fixed in 2001. Considering CO_2 concentrations, the trend of global GPP interannual change increased by 60.6%. As the fuel of photosynthesis, a continued rise in atmospheric CO_2 contributed positively to the increase in GPP [25,82]. In this study, atmospheric CO_2 concentrations cumulatively contributed 30.77 Pg C to the global GPP simulation based on the NI-LUE model from 2001 to 2018. For the spatial pattern of the cumulative contribution of CO_2 to GPP simulation from 2001 to 2018 (Figure 16b), it is similar to the global vegetation distribution, with higher contributions in tropical Southeast Asia, central Africa and South America, decreasing from low latitudes to high latitudes.

LAI was mainly used in the NI-LUE model to distinguish shaded leaves and sunlit leaves, and calculate their APAR. With the LAI fixed in 2001, the global NI-LUE_{LAI0} GPP still showed a significant increasing trend with a rate of 0.53 Pg C/yr. Overall, the cumulative contribution of LAI to global GPP from 2001 to 2018 was -8.12 Pg C. It was obvious that, from 2006 to 2009 and 2018, LAI played an important role in the reduction of global GPP simulations based on the NI-LUE model (Figure 15). For the spatial pattern of cumulative contributions to LAI (Figure 16c), the positive contribution of LAI was mainly distributed in northeast China, central and southern North America, and central Brazil, while the negative contribution of LAI was obvious in southern Brazil, southeastern Africa, and Australia. It was worth noting that the contribution of LAI was most likely to depend on the LAI product driving the model, and its initial value in 2001 may determine the contribution to GPP.

Keeping the land cover in its initial state had little effect on the global GPP simulation, with the NI-LUE_{LC0} GPP increasing at a rate of 0.54 Pg C/yr. The contribution of land cover changes to GPP from 2001 to 2018 was only −1.88 PgC. Figure 16d showed that the contribution of land cover was concentrated near the equator. In East South America, Central Africa, Central Europe, and Southeast Asia, land cover made a significant negative contribution.

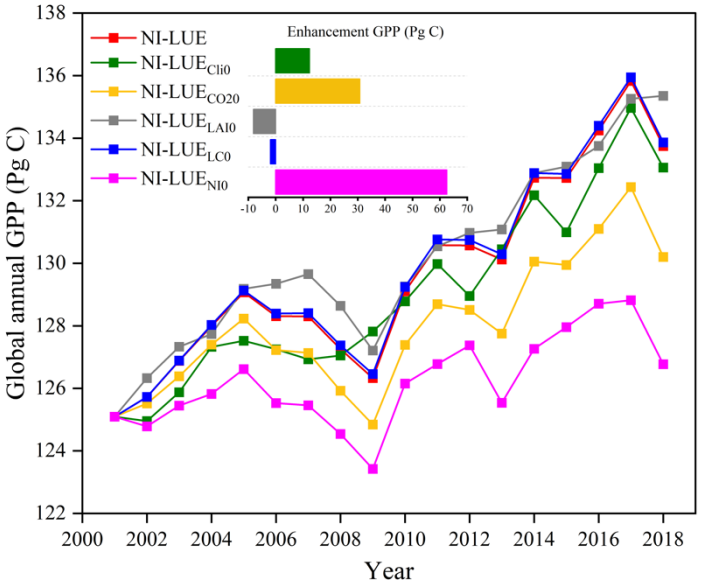

Figure 15. Interannual variation of the global annual total GPP (NI-LUE$_{i0}$) with variable *i* fixed at the initial state.

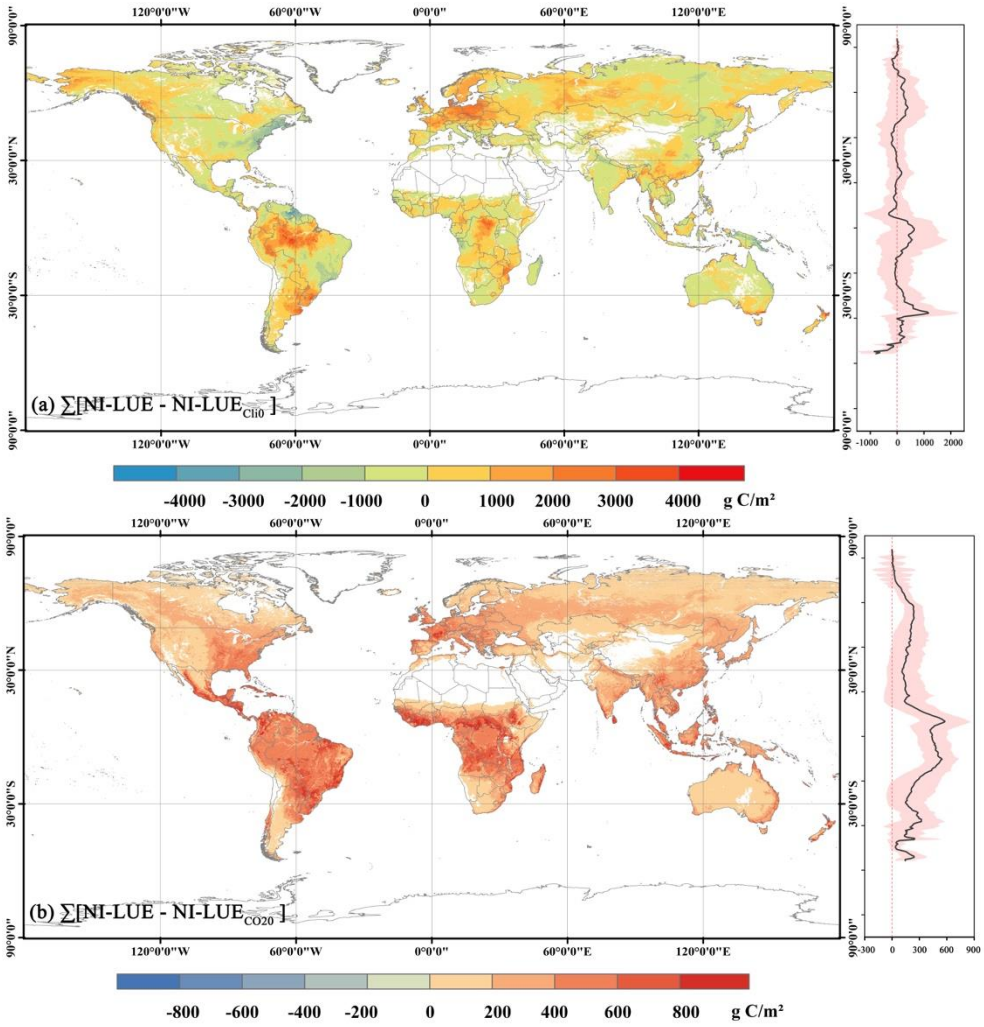

Figure 16. *Cont.*

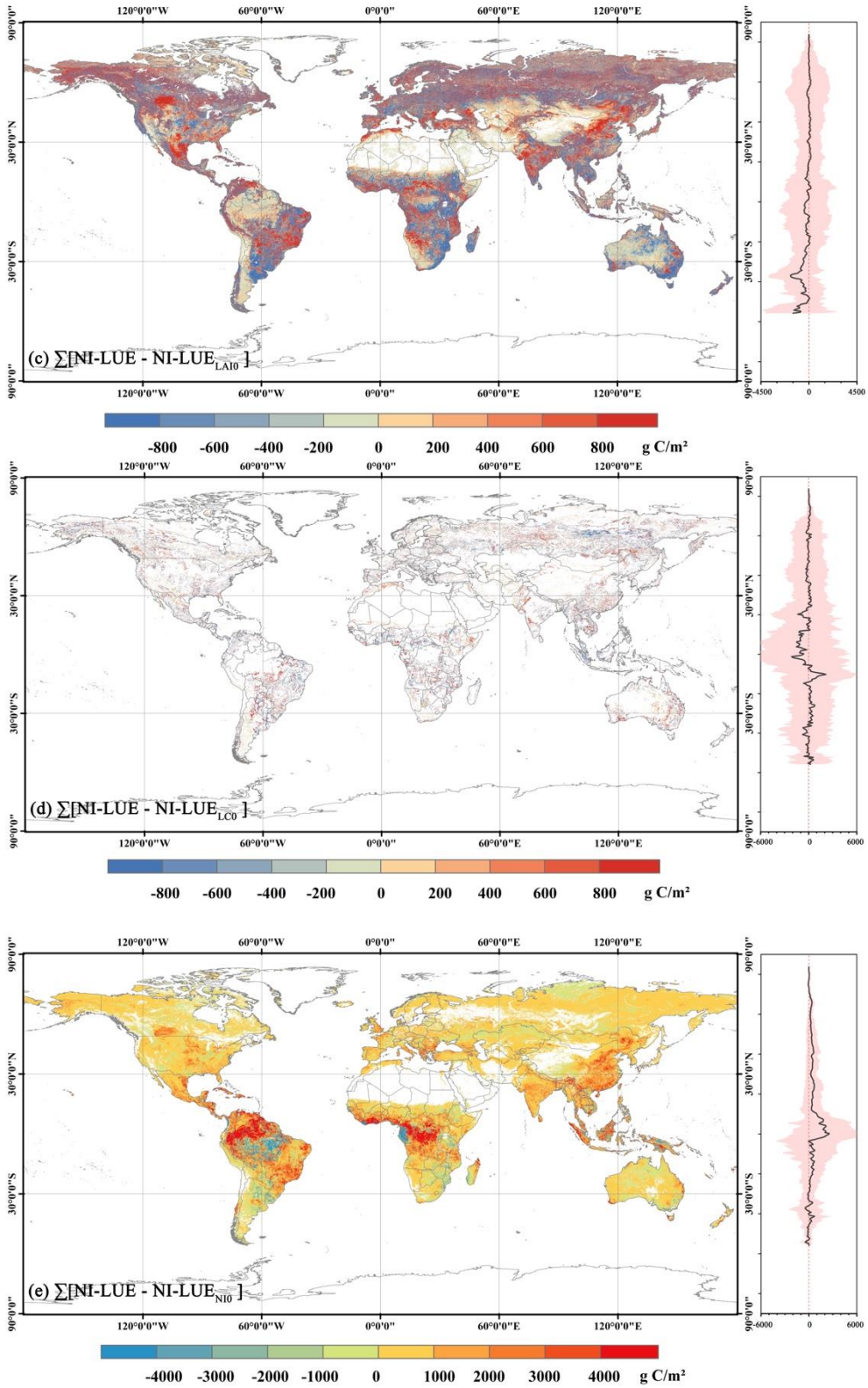

Figure 16. Spatial patterns of cumulative contributions of various variables to global annual GPP from 2001 to 2018. (**a**) Climate variables; (**b**) atmospheric CO_2 concentrations; (**c**) Leaf area index (LAI); (**d**) Land cover (LC); (**e**) Nitrogen index (NI).

CI_{green}, an index to characterize the canopy N concentrations (NI) in the NI-LUE model, was used to calculate dynamic ε_{max}, which had a significant impact on global GPP

simulations. The seasonal variability of the ε_{max} in the LUE model could make the model more suitable because the foliage responds adaptively to the seasonal fluctuations in the environmental conditions [47]. In this study, we used satellite reflectance to calculate NI, and although N itself may not be the only variable driving the observed pattern, leaf N concentrations influence leaf traits related to photosynthetic capacity that affect reflectance [53]. Canopy N concentrations may explain the temporal and spatial variation of the ε_{max} [46]. In fact, the ε_{max} is a large source of uncertainty. Even for the same vegetation, the ε_{max} may be different [83]. Fixing NI at the initial state in 2001, the increasing rate of the global NI-LUE$_{NI0}$ GPP, from 2001 to 2018, was significantly lower than that of the original NI-LUE GPP, at 0.19 Pg C/yr. Moreover, NI contributed 62.55 Pg C cumulatively to global GPP simulations from 2001 to 2018. The cumulative contribution of NI was concentrated in northern South America, central Africa, southeastern China, and Southeast Asia.

5.2. Uncertainties Analysis

In general, the photosynthesis of the C4 and C3 plants under the same conditions is quite different [84]. In our model, the same coefficients of C3/C4 plants may cause uncertainties. In future research, we may need fine biotype products to optimize the parameters of C3/C4 vegetation separately, which would be beneficial in avoiding some uncertainties for cropland and grassland [84,85].

In this study, CI$_{green}$ was selected as the nitrogen index to characterize the canopy N concentrations, but there were still many vegetation indices that we did not consider. For example, regarding Medium Resolution Imaging Spectrometer (MERIS) Terrestrial Chlorophyll Index (MTCI) and Double-peak Canopy Index (DCNI), previous studies demonstrated that these indices performed well in estimating canopy N concentrations [51,86]. However, the spectral resolution of the sensors and the time span of the available data prevented us from applying these indices to global long time-series studies. In addition, there are many vegetation parameters that have the potential to be applied to the model to adjust the ε_{max}, such as LAI and leaf chlorophyll content. These parameters related to the photosynthetic capacity of vegetation are worthy of further exploration.

The spatial resolution of NI-LUE GPP products is 0.05°, which mainly depends on the input LAI and land cover data. However, land cover changes within a pixel cannot change the main land use type of the pixel, which may not fully reflect the impact of land cover on GPP. Moreover, the footprint of flux sites is around 500~2000 m [87]. Although we screened for flux sites with lower heterogeneity of the underlying surface, there was still a scale mismatch between the input data and flux sites, which may lead to uncertainties in parameter optimization and accuracy verification. Future research may need to develop a method for mixed pixels to optimize parameters.

5.3. Potential Benefits and Applications of the Product

This study showed that the NI-LUE GPP had a high consistency with the FLUXNET GPP. The comparison of NI-LUE GPP with other GPP products also reflected the rationality of the interannual variation and spatial pattern of NI-LUE GPP. The above results suggest that NI-LUE GPP has the potential to complement current global GPP products.

In terms of analyzing global or regional GPP spatial patterns, NI-LUE GPP may discover valuable insights that have not been found in other products due to the consideration of the spatial heterogeneity of optimal temperature and ε_{max}.

Since the NI-LUE model simultaneously considered temperature, water, radiation components, atmospheric CO_2 concentrations, and NI, NI-LUE GPP could be used in both long-term GPP trend analysis and change detection. It may have great potential and may help us to identify and quantify the drivers affecting the long-term GPP trends.

In addition, there are significant differences among the many current global GPP products (Figure 13a). Like these global GPP products, NI-LUE GPP cannot be regarded as the actual value of GPP, but it can be used as a new global GPP dataset for compar-

ison with other products or models, which helps to understand the performance of the dataset comprehensively.

6. Conclusions

In this study, we produced a global GPP product at 8-day intervals with a spatial resolution of 0.05° from 2001 to 2018, based on an improved LUE model that simultaneously considered temperature, water, atmospheric CO_2 concentrations, radiative composition, and canopy N concentrations. Moreover, the spatial heterogeneity of optimum temperatures was considered when calculating temperature stress. CI_{green} was introduced into the model as a vegetation index characterizing the canopy N concentrations to achieve spatiotemporally dynamic ε_{max}, which more agrees with the adaptation of leaf photosynthesis to the environment. Validated by FLUXNET GPP, our product performed well on both daily and yearly scales. Further comparisons with other state-of-the-art global GPP products indicated that our GPP product has a reasonable long-term interannual variation and spatial patterns. Overall, this product provides an effective and alternative dataset for capturing spatiotemporal dynamics of GPP at the regional or global scale, and has the potential to assess the response of vegetaion to changes in the climate.

7. Data Availability

The NI-LUE GPP with 0.05° spatial resolution and at 8-day intervals from 2001 to 2018 and its uncertainty data can be accessed at https://zenodo.org/record/7057843.

Author Contributions: H.Z. developed the model, generated the product and wrote the original draft. J.B., Y.W. and Y.P. provided help for writing and coding. P.C.M. and Z.X. assisted in completing the verification and comparison. R.S. provided help for improvement of the model and writing of the draft. All authors have read and agreed to the published version of the manuscript.

Funding: This work was supported by the National Natural Science Foundation of China (42271330) and the National Key R&D Program of China (2017YFA0603002).

Institutional Review Board Statement: Not applicable.

Informed Consent Statement: Not applicable.

Acknowledgments: We thank NASA for providing the MODIS reflectance products (MCD43A4 & MYDOCGA) and all fluxnet communities of the eddy covariance data (FLUXNET2015, https://fluxnet.fluxdata.org/data/ (accessed on 11 October 2022)). We thank Martin Jung for providing FLUXCOM GPP products. We also thank Almut Arneth and Peter Anthony for providing LPJ-GUESS GPP products. We are grateful to Mikko Peltoniemi, Scott V. Ollinger, Takagi Kentaro, and Jeffrey M. Klopatek for the canopy nitrogen concentrations data. We also thank the anonymous reviewers for their helpful suggestions on the manuscript.

Conflicts of Interest: The authors declare no conflict of interest.

Appendix A

Table A1. Published vegetation indices evaluated in this study.

Index	Formulation	Selected MODIS Bands	References
Normalized difference vegetation index (NDVI)	$(R800 - R680)/(R800 + R680)$	B2 B1	Rouse et al. [88]
Simple ratio (SR)	$R800/R680$	B2 B1	Jordan [89]
Green NDVI (GNDVI)	$(R750 - R550)/(R750 + R550)$	B2 B4	Gitelson et al. [90]
Optimized soil-adjusted vegetation index (OSAVI)	$1.16 \times \frac{R800-R670}{R800+R670+0.16}$	B2 B1	Rondeaux et al. [91]
Structure insensitive pigment index (SIPI)	$(R800 - R455)/(R800 + R680)$	B2 B3 B1	Penuelas et al. [92]
Greenness index (GI)	$R554/R677$	B4 B1	Zarco-Tejada et al. [93]

Table A1. *Cont.*

Index	Formulation	Selected MODIS Bands	References
Green chlorophyll index (CI_{green})	$(R780/R550) - 1$	B2 B4	Gitelson et al. [94]
Modified transformed Chlorophyll absorption in reflectance index (TCARI)	$3 \times [(R800 - R680) - 0.2 \times (R680 - R550)] \times \frac{R800}{R680}$	B2 B1 B4	Rondeaux et al. [91]
TCARI/OSAVI	TCARI/OSAVI	B2 B1 B4	Rondeaux et al. [91]
Enhanced vegetation index 2 (EVI2)	$\frac{2.5 \times (R800 - R680)}{R800 + 2.4 \times R680 + 1}$	B2 B1	Jiang et al. [95]
Wide dynamic range vegetation index (WDRVI)	$(0.1 \times R800 - R670)/(0.1 \times R800 + R670)$	B2 B1	Gitelson [96]
Wide dynamic range vegetation index 3 (WDRVI3)	$\frac{0.2 \times R800 - R670}{0.2 \times R800 + R670} + 0.667$	B2 B1	Peng and Gitelson [97]
Modified simple ratio (MSR)	$\frac{\frac{R800}{R670} - 1}{\sqrt{\frac{R800}{R670} + 1}}$	B2 B1	Chen [98]
Plant pigment ratio (PPR)	$\frac{R550 - R450}{R550 + R450}$	B4 B3	Metternicht [99]
NIR	R800	B2	Ollinger et al. [53]
SPVI	$0.4 \times [3.7 \times (R800 - R670) - 1.2 \times \lvert R550 - R670 \rvert]$	B2 B1 B4	Vincini et al. [100]
Lichtenthaler Index 2 (LIC2)	$R440/R690$	B3 B1	Lichtenthaler et al. [101]
Enhanced vegetation index (EVI)	$\frac{2.5 \times (R800 - R680)}{R800 + 6 \times R680 - 7.5 \times R460 + 1}$	B2 B1 B3	Huete et al. [102]
Difference vegetation index (DVI)	$R800 - R680$	B2 B1	Jordan [89]
Modified Triangular Vegetation Index (MTVI)	$1.2 \times [1.2 \times (R800 - R550) - 2.5 \times (R670 - R550)]$	B2 B4 B1	Haboudane et al. [103]
NIRv	$NDVI \times NIR$	B1 B2	Badgley et al. [104]
kNDVI	$\tanh\left(NDVI^2\right)$	B1 B2	Camps-Valls et al. [105]
Chlorophyll/Carotenoid index (CCI)	$(B11 - B1)/(B11 + B1)$	B11 B1	Gamon et al. [106]

Table A2. Canopy N concentrations collected from previous studies.

Site	Latitude (°)	Longitude (°)	Canopy N, % by Mass	Vegetation Type	Date	References
Bartlett Experimental Forest, NH	44.05	−70.72	1.66	Mixed northern hardwood	Growing season between 2000 and 2006	Ollinger et al. [53]
Duke Forest Deciduous, NC	35.97	−78.90	1.85	Oak–hickor		
Duke Forest Pine, NC	35.97	−78.92	1.47	Loblolly pine		
Harvard Forest, MA	42.53	−71.83	1.95	Mixed deciduous		
Howland, ME	45.20	−67.27	1.16	Boreal evergreen		
Hubbard Brook, NH	43.95	−70.27	2.24	Northern hardwoods		
Morgan Monroe State Forest, IN	39.32	−85.60	2.06	Mixed deciduous		
Niwot Ridge, CO	40.02	−104.47	0.93	Subalpine evergreen		
Tremper Mount, NY	42.08	−73.73	2.35	Mixed deciduous		
Willow Creek, WI	45.80	−89.93	1.79	Temperate deciduous		
Wind River Experimental Forest, WA	45.82	−120.05	0.75	Temperate evergreen		
Hyytiälä, Finland, HY	61.85	24.30	1.2	Coniferous	Spring 2003	Peltoniemi et al. [46]
Abisko, Sweden, AB	68.35	18.78	1.79	Deciduous	Jul., Aug. 2003	Peltoniemi et al. [46]
Sorø, Denmark, SO	55.48	11.63	2.3	Mixed	Summer 2007	Peltoniemi et al. [46]
Teshio, Japan, TE	45.05	142.10	1.63	Mixed	Aug. 2001, Aug. 2002, Aug. 2003	Peltoniemi et al. [46]; Takagi et al. [107]
Wind River, USA, WR	45.82	−120.05	1.11	Coniferous	Sep. 2003	Peltoniemi et al. [46]; Klopatek et al. [108]

Table A3. Optimized parameters of the NI-LUE model for different vegetation types.

	CRO	DBF	EBF	ENF	MF	GRA	WSA	SAV	CSH	OSH	WET
p	0.31335	0.07883	0.29767	0.00002	0.00019	0.52879	0.18511	0.31125	0.32329	0.24062	0.78899
q	0.57816	1.26957	0.13659	1.73640	1.61985	0.00011	0.91392	1.03839	0.48866	0.33551	0.00002
a	0.00002	0.00092	0.00001	0.07253	0.00016	0.01613	0.01487	0.00814	0.00513	0.05444	0.92145

Table A4. FLUXNET sites used in this study.

SiteID	SiteName	Latitude	Longitude	IGBP	Study Period
AR−SLu	San Luis	−33.46	−66.46	MF	2009−2011
AU−ASM	Alice Springs	−22.28	133.25	SAV	2010−2014
AU−Cpr	Calperum	−34.00	140.59	SAV	2010−2014
AU−DaS	Daly River Cleared	−14.16	131.39	SAV	2008−2014
AU−Dry	Dry River	−15.26	132.37	SAV	2008−2014
AU−Gin	Gingin	−31.38	115.71	WSA	2011−2014
AU−GWW	Great Western Woodlands, Western Australia, Australia	−30.19	120.65	SAV	2013−2014
AU−How	Howard Springs	−12.49	131.15	WSA	2001−2014
AU−Rig	Riggs Creek	−36.65	145.58	GRA	2011−2014
AU−Stp	Sturt Plains	−17.15	133.35	GRA	2008−2014
AU−Tum	Tumbarumba	−35.66	148.15	EBF	2001−2014
AU−Wac	Wallaby Creek	−37.43	145.19	EBF	2005−2008
AU−Ync	Jaxa	−34.99	146.29	GRA	2012−2014
BE−Lon	Lonzee	50.55	4.75	CRO	2004−2014
BE−Vie	Vielsalm	50.30	6.00	MF	2001−2014
BR−Sa1	Santarem−Km67−Primary Forest	−2.86	−54.96	EBF	2002−2011
CA−Gro	Ontario—Groundhog River, Boreal Mixedwood Forest	48.22	−82.16	MF	2003−2014
CA−Man	Manitoba—Northern Old Black Spruce	55.88	−98.48	ENF	2001−2008
CA−NS1	UCI−1850 burn site	55.88	−98.48	ENF	2001−2005
CA−NS2	UCI−1930 burn site	55.91	−98.52	ENF	2001−2005
CA−NS3	UCI−1964 burn site	55.91	−98.38	ENF	2001−2005
CA−NS4	UCI−1964 burn site wet	55.91	−98.38	ENF	2002−2005
CA−NS5	UCI−1981 burn site	55.86	−98.49	ENF	2001−2005
CA−NS6	UCI−1989 burn site	55.92	−98.96	OSH	2001−2005
CA−NS7	UCI−1998 burn site	56.64	−99.95	OSH	2002−2005
CA−Oas	Saskatchewan—Western Boreal, Mature Aspen	53.63	−106.20	DBF	2001−2010
CA−Obs	Saskatchewan—Western Boreal, Mature Black Spruce	53.99	−105.12	ENF	2001−2010
CA−Qfo	Quebec—Eastern Boreal, Mature Black Spruce	49.69	−74.34	ENF	2003−2010
CA−SF1	Saskatchewan—Western Boreal, forest burned in 1977	54.49	−105.82	ENF	2003−2006
CA−SF2	Saskatchewan—Western Boreal, forest burned in 1989	54.25	−105.88	ENF	2001−2005
CA−SF3	Saskatchewan—Western Boreal, forest burned in 1998	54.09	−106.01	OSH	2001−2006
CH−Dav	Davos	46.82	9.86	ENF	2001−2014
CN−Cha	Changbaishan	42.40	128.10	MF	2003−2005
CN−Dan	Dangxiong	30.50	91.07	GRA	2004−2005
CN−Du2	Duolun_grassland (D01)	42.05	116.28	GRA	2006−2008
CN−Du3	Duolun Degraded Meadow	42.06	116.28	GRA	2009−2010
CN−Ha2	Haibei Shrubland	37.61	101.33	WET	2003−2005
CN−HaM	Haibei Alpine Tibet site	37.37	101.18	GRA	2002−2004
DE−Geb	Gebesee	51.10	10.91	CRO	2001−2014
DE−Hai	Hainich	51.08	10.45	DBF	2001−2012
DE−Kli	Klingenberg	50.89	13.52	CRO	2004−2014
DE−RuS	Selhausen Juelich	50.87	6.45	CRO	2011−2014
DE−SfN	Schechenfilz Nord	47.81	11.33	WET	2012−2014
DE−Spw	Spreewald	51.89	14.03	WET	2010−2014
DE−Zrk	Zarnekow	53.88	12.89	WET	2013−2014
DK−Fou	Foulum	56.48	9.59	CRO	2005
ES−Amo	Amoladeras	36.83	−2.25	OSH	2007−2012
ES−LgS	Laguna Seca	37.10	−2.97	OSH	2007−2009
ES−LJu	Llano de los Juanes	36.93	−2.75	OSH	2004−2013

Table A4. *Cont.*

SiteID	SiteName	Latitude	Longitude	IGBP	Study Period
ES−Ln2	Lanjaron−Salvage logging	36.97	−3.48	OSH	2009−2009
FR−Gri	Grignon	48.84	1.95	CRO	2004−2014
FR−Pue	Puechabon	43.74	3.60	EBF	2001−2014
IT−BCi	Borgo Cioffi	40.52	14.96	CRO	2004−2014
IT−Col	Collelongo	41.85	13.59	DBF	2001−2014
IT−Noe	Arca di Noe—Le Prigionette	40.61	8.15	CSH	2004−2014
IT−Ren	Renon	46.59	11.43	ENF	2001−2013
JP−MBF	Moshiri Birch Forest Site	44.39	142.32	DBF	2003−2005
JP−SMF	Seto Mixed Forest Site	35.26	137.08	MF	2002−2006
MY−PSO	Pasoh Forest Reserve (PSO)	2.97	102.31	EBF	2003−2009
NL−Hor	Horstermeer	52.24	5.07	GRA	2004−2011
RU−Che	Cherski	68.61	161.34	WET	2002−2005
RU−Ha1	Hakasia steppe	54.73	90.00	GRA	2002−2004
RU−SkP	Yakutsk Spasskaya Pad larch	62.26	129.17	DNF	2012−2014
RU−Tks	Tiksi	71.59	128.89	GRA	2010−2014
RU−Vrk	Seida/Vorkuta	67.05	62.94	CSH	2008−2008
SD−Dem	Demokeya	13.28	30.48	SAV	2005−2009
SN−Dhr	Dahra	15.40	−15.43	SAV	2010−2013
US−AR1	ARM USDA UNL OSU Woodward Switchgrass 1	36.43	−99.42	GRA	2009−2012
US−ARb	ARM Southern Great Plains burn site− Lamont	35.55	−98.04	GRA	2005−2006
US−ARM	ARM Southern Great Plains site− Lamont	36.61	−97.49	CRO	2003−2012
US−Atq	Atqasuk	70.47	−157.41	WET	2003−2008
US−Blo	Blodgett Forest	38.90	−120.63	ENF	2001−2007
US−Cop	Corral Pocket	38.09	−109.39	GRA	2001−2007
US−CRT	Curtice Walter−Berger cropland	41.63	−83.35	CRO	2011−2013
US−Ha1	Harvard Forest EMS Tower (HFR1)	42.54	−72.17	DBF	2001−2012
US−Ivo	Ivotuk	68.49	−155.75	WET	2004−2007
US−KS2	Kennedy Space Center (scrub oak)	28.61	−80.67	CSH	2003−2006
US−Lin	Lindcove Orange Orchard	36.36	−119.09	CRO	2009−2010
US−Los	Lost Creek	46.08	−89.98	WET	2001−2014
US−Me1	Metolius—Eyerly burn	44.58	−121.50	ENF	2004−2005
US−Me2	Metolius mature ponderosa pine	44.45	−121.56	ENF	2002−2014
US−Me3	Metolius−second young aged pine	44.32	−121.61	ENF	2004−2009
US−Me6	Metolius Young Pine Burn	44.32	−121.61	ENF	2010−2014
US−MMS	Morgan Monroe State Forest	39.32	−86.41	DBF	2001−2014
US−Ne1	Mead—irrigated continuous maize site	41.17	−96.48	CRO	2001−2013
US−Ne2	Mead—irrigated maize−soybean rotation site	41.16	−96.47	CRO	2001−2013
US−Ne3	Mead—rainfed maize−soybean rotation site	41.18	−96.44	CRO	2001−2013
US−NR1	Niwot Ridge Forest (LTER NWT1)	40.03	−105.55	ENF	2001−2014
US−PFa	Park Falls/WLEF	45.95	−90.27	MF	2001−2014
US−SRC	Santa Rita Creosote	31.91	−110.84	OSH	2008−2014
US−SRM	Santa Rita Mesquite	31.82	−110.87	WSA	2004−2014
US−Sta	Saratoga	41.40	−106.80	OSH	2005−2009
US−Ton	Tonzi Ranch	38.43	−120.97	WSA	2001−2014
US−UMB	Univ. of Mich. Biological Station	45.56	−84.71	DBF	2001−2014
US−UMd	UMBS Disturbance	45.56	−84.70	DBF	2007−2014
US−WCr	Willow Creek	45.81	−90.08	DBF	2001−2014
US−Whs	Walnut Gulch Lucky Hills Shrub	31.74	−110.05	OSH	2007−2014
US−Wi4	Mature red pine (MRP)	46.74	−91.17	ENF	2002−2005
US−Wi9	Young Jack pine (YJP)	46.74	−91.07	ENF	2002
US−Wkg	Walnut Gulch Kendall Grasslands	31.74	−109.94	GRA	2002
ZA−Kru	Skukuza	−25.02	31.50	SAV	2002
ZM−Mon	Mongu	−15.44	23.25	DBF	2002

References

1. Beer, C.; Reichstein, M.; Tomelleri, E.; Ciais, P.; Jung, M.; Carvalhais, N.; Rödenbeck, C.; Arain, M.A.; Baldocchi, D.; Bonan, G.B.; et al. Terrestrial Gross Carbon Dioxide Uptake: Global Distribution and Covari-ation with Climate. *Science* **2010**, *329*, 834–838. [CrossRef] [PubMed]
2. Bonan, G.B.; Lombardozzi, D.L.; Wieder, W.R.; Oleson, K.W.; Lawrence, D.M.; Hoffman, F.M.; Collier, N. Model Structure and Climate Data Uncertainty in Historical Simulations of the Terrestrial Carbon Cycle (1850–2014). *Glob. Biogeochem. Cycles* **2019**, *33*, 1310–1326. [CrossRef]
3. Guan, X.; Chen, J.M.; Shen, H.; Xie, X. A modified two-leaf light use efficiency model for improving the simulation of GPP using a radiation scalar. *Agric. For. Meteorol.* **2021**, *307*, 108546. [CrossRef]
4. Huang, X.; Xiao, J.; Wang, X.; Ma, M. Improving the global MODIS GPP model by optimizing parameters with FLUXNET data. *Agric. For. Meteorol.* **2021**, *300*, 108314. [CrossRef]
5. Niyogi, D.; Jamshidi, S.; Smith, D.; Kellner, O. Evapotranspiration Climatology of Indiana Using In Situ and Remotely Sensed Products. *J. Appl. Meteorol. Clim.* **2020**, *59*, 2093–2111. [CrossRef]
6. Verma, M.; Friedl, M.; Law, B.; Bonal, D.; Kiely, G.; Black, T.; Wohlfahrt, G.; Moors, E.; Montagnani, L.; Marcolla, B.; et al. Improving the performance of remote sensing models for capturing intra- and inter-annual variations in daily GPP: An analysis using global FLUXNET tower data. *Agric. For. Meteorol.* **2015**, *214–215*, 416–429. [CrossRef]
7. Xiao, J.; Zhuang, Q.; Baldocchi, D.D.; Law, B.E.; Richardson, A.D.; Chen, J.; Oren, R.; Starr, G.; Noormets, A.; Ma, S.; et al. Estimation of net ecosystem carbon exchange for the conterminous United States by combining MODIS and AmeriFlux data. *Agric. For. Meteorol.* **2008**, *148*, 1827–1847. [CrossRef]
8. Sharpe, D.M. Methods of Assessing the Primary Production of Regions. In *Primary Productivity of the Biosphere*; Lieth, H., Whittaker, R.H., Eds.; Springer: Berlin/Heidelberg, Germany, 1975; pp. 147–166.
9. Uchijima, Z.; Seino, H. Agro climatic evaluation of net primary productivity of natural vegetation I. Chikugo model for evaluating productivity. *J. Agric. Meteorol.* **1985**, *40*, 343–352. [CrossRef]
10. Hunt, E.R., Jr.; Piper, S.C.; Nemani, R.; Keeling, C.D.; Otto, R.D.; Running, S.W. Global net carbon exchange and intra-annual atmospheric CO2 concentrations predicted by an ecosystem process model and three-dimensional atmospheric transport model. *Glob. Biogeochem. Cycles* **1996**, *10*, 431–456. [CrossRef]
11. Liu, J.; Chen, J.M.; Cihlar, J.; Park, W.M. A process-based boreal ecosystem productivity simulator using remote sensing inputs. *Remote Sens. Environ.* **1997**, *62*, 158–175. [CrossRef]
12. Melillo, J.M.; McGuire, A.D.; Kicklighter, D.W.; Moore, B.; Vorosmarty, C.J.; Schloss, A.L. Global climate change and terrestrial net primary production. *Nature* **1993**, *363*, 234–240. [CrossRef]
13. Running, S.W.; Coughlan, J.C. A general model of forest ecosystem processes for regional applications I. Hydrologic balance, canopy gas exchange and primary production processes. *Ecol. Model.* **1988**, *42*, 125–154. [CrossRef]
14. He, M.; Ju, W.; Zhou, Y.; Chen, J.; He, H.; Wang, S.; Wang, H.; Guan, D.; Yan, J.; Li, Y.; et al. Development of a two-leaf light use efficiency model for improving the calculation of terrestrial gross primary productivity. *Agric. For. Meteorol.* **2013**, *173*, 28–39. [CrossRef]
15. Heinsch, F.A.; Reeves, M.; Votava, P.; Kang, S.; Milesi, C.; Zhao, M.; Glassy, J.; Jolly, W.M.; Loehman, R.; Bowker, C.F.; et al. User's guide GPP and NPP (MOD17A2/A3) products NASA MODIS land algorithm. *Version* **2003**, *2*, 666–684.
16. Monteith, J.L. Solar Radiation and Productivity in Tropical Ecosystems. *J. Appl. Ecol.* **1972**, *9*, 747–766. [CrossRef]
17. Monteith, J.L. Climate and the efficiency of crop production in Britain. *Philos. Trans. R. Soc. London. B Biol. Sci.* **1977**, *281*, 277–294.
18. Potter, C.S.; Randerson, J.T.; Field, C.B.; Matson, P.A.; Vitousek, P.M.; Mooney, H.A.; Klooster, S.A. Terrestrial ecosystem production: A process model based on global satellite and surface data. *Glob. Biogeochem. Cycles* **1993**, *7*, 811–841. [CrossRef]
19. Wang, J.; Sun, R.; Zhang, H.; Xiao, Z.; Zhu, A.; Wang, M.; Yu, T.; Xiang, K. New Global MuSyQ GPP/NPP Remote Sensing Products From 1981 to 2018. *IEEE J. Sel. Top. Appl. Earth Obs. Remote Sens.* **2021**, *14*, 5596–5612. [CrossRef]
20. Xiao, X.; Zhang, Q.; Braswell, B.; Urbanski, S.; Boles, S.; Wofsy, S.; Moore, B., III; Ojima, D. Modeling gross primary production of temperate deciduous broadleaf forest using satellite images and climate data. *Remote Sens. Environ.* **2004**, *91*, 256–270. [CrossRef]
21. Alemohammad, S.H.; Fang, B.; Konings, A.G.; Aires, F.; Green, J.K.; Kolassa, J.; Miralles, D.; Prigent, C.; Gentine, P. Water, Energy, and Carbon with Artificial Neural Networks (WECANN): A statistically based estimate of global surface turbulent fluxes and gross primary productivity using solar-induced fluorescence. *Biogeosciences* **2017**, *14*, 4101–4124. [CrossRef]
22. Dou, X.; Yang, Y. Estimating forest carbon fluxes using four different data-driven techniques based on long-term eddy covariance measurements: Model comparison and evaluation. *Sci. Total Environ.* **2018**, *627*, 78–94. [CrossRef] [PubMed]
23. Ichii, K.; Ueyama, M.; Kondo, M.; Saigusa, N.; Kim, J.; Alberto, M.C.; Ardö, J.; Euskirchen, E.S.; Kang, M.; Hirano, T.; et al. New data-driven estimation of terrestrial CO2 fluxes in Asia using a stand-ardized database of eddy covariance measurements, remote sensing data, and support vector regression. *J. Geophys. Res. Biogeosciences* **2017**, *122*, 767–795. [CrossRef]
24. Xiao, J.; Ollinger, S.V.; Frolking, S.; Hurtt, G.C.; Hollinger, D.Y.; Davis, K.J.; Pan, Y.; Zhang, X.; Deng, F.; Chen, J.; et al. Data-driven diagnostics of terrestrial carbon dynamics over North America. *Agric. For. Meteorol.* **2014**, *197*, 142–157. [CrossRef]
25. Bao, S.; Wutzler, T.; Koirala, S.; Cuntz, M.; Ibrom, A.; Besnard, S.; Walther, S.; Šigut, L.; Moreno, A.; Weber, U.; et al. Environment-sensitivity functions for gross primary productivity in light use efficiency models. *Agric. For. Meteorol.* **2022**, *312*, 108708. [CrossRef]

26. Zheng, Y.; Shen, R.; Wang, Y.; Li, X.; Liu, S.; Liang, S.; Chen, J.M.; Ju, W.; Zhang, L.; Yuan, W. Improved estimate of global gross primary production for reproducing its long-term variation, 1982–2017. *Earth Syst. Sci. Data* **2020**, *12*, 2725–2746. [CrossRef]
27. Dechant, B.; Cuntz, M.; Vohland, M.; Schulz, E.; Doktor, D. Estimation of photosynthesis traits from leaf reflectance spectra: Correlation to nitrogen content as the dominant mechanism. *Remote Sens. Environ.* **2017**, *196*, 279–292. [CrossRef]
28. Stocker, B.D.; Zscheischler, J.; Keenan, T.F.; Prentice, I.C.; Seneviratne, S.I.; Peñuelas, J. Drought impacts on terrestrial primary production underestimated by satellite monitoring. *Nat. Geosci.* **2019**, *12*, 264–270. [CrossRef]
29. Medlyn, B.E.; Dreyer, E.; Ellsworth, D.; Forstreuter, M.; Harley, P.C.; Kirschbaum, M.U.F.; LE Roux, X.; Montpied, P.; Strassemeyer, J.; Walcroft, A.; et al. Temperature response of parameters of a biochemically based model of photosynthesis. II. A review of experimental data. *Plant Cell Environ.* **2002**, *25*, 1167–1179. [CrossRef]
30. Chen, Y.; Feng, X.; Fu, B.; Wu, X.; Gao, Z. Improved Global Maps of the Optimum Growth Temperature, Maximum Light Use Efficiency, and Gross Primary Production for Vegetation. *J. Geophys. Res. Biogeosciences* **2021**, *126*, e2020JG005651. [CrossRef]
31. Liu, Y.; Piao, S.; Lian, X.; Ciais, P.; Smith, W.K. Seasonal Responses of Terrestrial Carbon Cycle to Climate Variations in CMIP5 Models: Evaluation and Projection. *J. Clim.* **2017**, *30*, 6481–6503. [CrossRef]
32. Yang, D.; Xu, X.; Xiao, F.; Xu, C.; Luo, W.; Tao, L. Improving modeling of ecosystem gross primary productivity through re-optimizing temperature restrictions on photosynthesis. *Sci. Total Environ.* **2021**, *788*, 147805. [CrossRef]
33. Huang, M.; Piao, S.; Ciais, P.; Peñuelas, J.; Wang, X.; Keenan, T.F.; Peng, S.; Berry, J.A.; Wang, K.; Mao, J.; et al. Air temperature optima of vegetation productivity across global biomes. *Nat. Ecol. Evol.* **2019**, *3*, 772–779. [CrossRef]
34. Niu, S.; Luo, Y.; Fei, S.; Yuan, W.; Schimel, D.; Law, B.; Ammann, C.; Arain, M.A.; Arneth, A.; Aubinet, M.; et al. Thermal optimality of net ecosystem exchange of carbon dioxide and underlying mechanisms. *New Phytol.* **2012**, *194*, 775–783. [CrossRef]
35. Veroustraete, F.; Sabbe, H.; Eerens, H. Estimation of carbon mass fluxes over Europe using the C-Fix model and Euroflux data. *Remote Sens. Environ.* **2002**, *83*, 376–399. [CrossRef]
36. Stocker, B.D.; Wang, H.; Smith, N.G.; Harrison, S.P.; Keenan, T.F.; Sandoval, D.; Davis, T.; Prentice, I.C. P-model v1.0: An optimality-based light use efficiency model for simulating ecosystem gross primary production. *Geosci. Model Dev.* **2020**, *13*, 1545–1581. [CrossRef]
37. Kalliokoski, T.; Mäkelä, A.; Fronzek, S.; Minunno, F.; Peltoniemi, M. Decomposing sources of uncertainty in climate change projections of boreal forest primary production. *Agric. For. Meteorol.* **2018**, *262*, 192–205. [CrossRef]
38. Chen, J.; Liu, J.; Cihlar, J.; Goulden, M. Daily canopy photosynthesis model through temporal and spatial scaling for remote sensing applications. *Ecol. Model.* **1999**, *124*, 99–119. [CrossRef]
39. Wang, S.; Huang, K.; Yan, H.; Yan, H.; Zhou, L.; Wang, H.; Zhang, J.; Yan, J.; Zhao, L.; Wang, Y.; et al. Improving the light use efficiency model for simulating terrestrial vegetation gross primary production by the inclusion of diffuse radiation across ecosystems in China. *Ecol. Complex.* **2015**, *23*, 1–13. [CrossRef]
40. He, J.; Zhang, X.; Guo, W.; Pan, Y.; Yao, X.; Cheng, T.; Zhu, Y.; Cao, W.; Tian, Y. Estimation of Vertical Leaf Nitrogen Distribution Within a Rice Canopy Based on Hyperspectral Data. *Front. Plant Sci.* **2020**, *10*, 1802. [CrossRef]
41. Loozen, Y.; Rebel, K.T.; de Jong, S.M.; Lu, M.; Ollinger, S.V.; Wassen, M.J.; Karssenberg, D. Mapping canopy nitrogen in European forests using remote sensing and environmental variables with the random forests method. *Remote Sens. Environ.* **2020**, *247*, 111933. [CrossRef]
42. Reich, P.B. Key canopy traits drive forest productivity. *Proc. R. Soc. B: Biol. Sci.* **2012**, *279*, 2128–2134. [CrossRef] [PubMed]
43. Lin, X.; Chen, B.; Chen, J.; Zhang, H.; Sun, S.; Xu, G.; Guo, L.; Ge, M.; Qu, J.; Li, L.; et al. Seasonal fluctuations of photosynthetic parameters for light use efficiency models and the impacts on gross primary production estimation. *Agric. For. Meteorol.* **2017**, *236*, 22–35. [CrossRef]
44. Zhou, X.; Xin, Q. Improving satellite-based modelling of gross primary production in deciduous broadleaf forests by accounting for seasonality in light use efficiency. *Int. J. Remote Sens.* **2019**, *40*, 931–955. [CrossRef]
45. Balzarolo, M.; Valdameri, N.; Fu, Y.H.; Schepers, L.; Janssens, I.A.; Campioli, M. Different determinants of radiation use efficiency in cold and temperate forests. *Glob. Ecol. Biogeogr.* **2019**, *28*, 1649–1667. [CrossRef]
46. Peltoniemi, M.; Pulkkinen, M.; Kolari, P.; Duursma, R.A.; Montagnani, L.; Wharton, S.; Lagergren, F.; Takagi, K.; Verbeeck, H.; Christensen, T.; et al. Does canopy mean nitrogen concentration explain variation in canopy light use efficiency across 14 contrasting forest sites? *Tree Physiol.* **2012**, *32*, 200–218. [CrossRef]
47. Houborg, R.; Anderson, M.C.; Norman, J.M.; Wilson, T.; Meyers, T. Intercomparison of a 'bottom-up' and 'top-down' modeling para-digm for estimating carbon and energy fluxes over a variety of vegetative regimes across the U.S. *Agric. For. Meteorol.* **2009**, *149*, 1875–1895. [CrossRef]
48. Butler, E.E.; Datta, A.; Flores-Moreno, H.; Chen, M.; Wythers, K.R.; Fazayeli, F.; Banerjee, A.; Atkin, O.K.; Kattge, J.; Amiaud, B.; et al. Mapping local and global variability in plant trait distributions. *Proc. Natl. Acad. Sci. USA* **2017**, *114*, E10937–E10946. [CrossRef]
49. Moreno-Martínez, Á.; Camps-Valls, G.; Kattge, J.; Robinson, N.; Reichstein, M.; van Bodegom, P.; Kramer, K.; Cornelissen, J.H.C.; Reich, P.; Bahn, M.; et al. A methodology to derive global maps of leaf traits using remote sensing and climate data. *Remote Sens. Environ.* **2018**, *218*, 69–88. [CrossRef]
50. Wen, P.; He, J.; Ning, F.; Wang, R.; Zhang, Y.; Li, J. Estimating leaf nitrogen concentration considering unsynchronized maize growth stages with canopy hyperspectral technique. *Ecol. Indic.* **2019**, *107*, 105590. [CrossRef]

51. Chen, P.; Haboudane, D.; Tremblay, N.; Wang, J.; Vigneault, P.; Li, B. New spectral indicator assessing the efficiency of crop nitrogen treatment in corn and wheat. *Remote Sens. Environ.* **2010**, *114*, 1987–1997. [CrossRef]
52. He, L.; Zhang, H.Y.; Zhang, Y.S.; Song, X.; Feng, W.; Kang, G.Z.; Wang, C.Y.; Guo, T.C. Estimating canopy leaf nitrogen concentration in winter wheat based on mul-ti-angular hyperspectral remote sensing. *Eur. J. Agron.* **2016**, *73*, 170–185. [CrossRef]
53. Ollinger, S.V.; Richardson, A.D.; Martin, M.E.; Hollinger, D.Y.; Frolking, S.E.; Reich, P.B.; Plourde, L.C.; Katul, G.G.; Munger, J.W.; Oren, R.; et al. Canopy nitrogen, carbon assimilation, and albedo in temperate and boreal forests: Functional relations and potential climate feedbacks. *Proc. Natl. Acad. Sci. USA* **2008**, *105*, 19336–19341. [CrossRef]
54. Ollinger, S.V.; Smith, M.-L. Net Primary Production and Canopy Nitrogen in a Temperate Forest Landscape: An Analysis Using Imaging Spectroscopy, Modeling and Field Data. *Ecosystems* **2005**, *8*, 760–778. [CrossRef]
55. Xiao, Z.; Liang, S.; Jiang, B. Evaluation of four long time-series global leaf area index products. *Agric. For. Meteorol.* **2017**, *246*, 218–230. [CrossRef]
56. Jacobson, A.R.; Schuldt, K.N.; Miller, J.B.; Oda, T.; Tans, P.; Andrews, A.; Mund, J.; Ott, L.; Collatz, G.J.; Aalto, T.; et al. *CarbonTracker CT2019B*; NOAA Global Monitoring Laboratory: Washington, DC, USA, 2020.
57. Savitzky, A.; Golay, M.J.E. Smoothing and Differentiation of Data by Simplified Least Squares Procedures. *Anal. Chem.* **1964**, *36*, 1627–1639. [CrossRef]
58. Zhang, Y.; Joiner, J.; Alemohammad, S.H.; Zhou, S.; Gentine, P. A global spatially contiguous solar-induced fluorescence (CSIF) dataset using neural networks. *Biogeosciences* **2018**, *15*, 5779–5800. [CrossRef]
59. Zhao, M.; Heinsch, F.A.; Nemani, R.R.; Running, S.W. Improvements of the MODIS terrestrial gross and net primary production global data set. *Remote Sens. Environ.* **2005**, *95*, 164–176. [CrossRef]
60. Zhang, Y.; Xiao, X.; Wu, X.; Zhou, S.; Zhang, G.; Qin, Y.; Dong, J. A global moderate resolution dataset of gross primary production of vegetation for 2000–2016. *Sci. Data* **2017**, *4*, 170165. [CrossRef]
61. Li, X.; Xiao, J. A Global, 0.05-Degree Product of Solar-Induced Chlorophyll Fluorescence Derived from OCO-2, MODIS, and Reanalysis Data. *Remote Sens.* **2019**, *11*, 517. [CrossRef]
62. Jung, M.; Schwalm, C.; Migliavacca, M.; Walther, S.; Camps-Valls, G.; Koirala, S.; Anthoni, P.; Besnard, S.; Bodesheim, P.; Carvalhais, N.; et al. Scaling carbon fluxes from eddy covariance sites to globe: Synthesis and evaluation of the FLUXCOM approach. *Biogeosciences* **2020**, *17*, 1343–1365. [CrossRef]
63. Smith, B.; Wårlind, D.; Arneth, A.; Hickler, T.; Leadley, P.; Siltberg, J.; Zaehle, S. Implications of incorporating N cycling and N limitations on primary pro-duction in an individual-based dynamic vegetation model. *Biogeosciences* **2014**, *11*, 2027–2054. [CrossRef]
64. Walker, A.P.; Quaife, T.; Van Bodegom, P.M.; De Kauwe, M.G.; Keenan, T.F.; Joiner, J.; Lomas, M.R.; MacBean, N.; Xu, C.; Yang, X.; et al. The impact of alternative trait-scaling hypotheses for the maximum photosynthetic carboxylation rate (Vcmax) on global gross primary production. *New Phytol.* **2017**, *215*, 1370–1386. [CrossRef] [PubMed]
65. Jamshidi, S.; Zand-Parsa, S.; Pakparvar, M.; Niyogi, D. Evaluation of Evapotranspiration over a Semiarid Region Using Multiresolution Data Sources. *J. Hydrometeorol.* **2019**, *20*, 947–964. [CrossRef]
66. Raoufi, R.; Beighley, E. Estimating Daily Global Evapotranspiration Using Penman–Monteith Equation and Remotely Sensed Land Surface Temperature. *Remote Sens.* **2017**, *9*, 1138. [CrossRef]
67. Cui, T.; Wang, Y.; Sun, R.; Qiao, C.; Fan, W.; Jiang, G.; Hao, L.; Zhang, L. Estimating Vegetation Primary Production in the Heihe River Basin of China with Multi-Source and Multi-Scale Data. *PLoS ONE* **2016**, *11*, e0153971. [CrossRef]
68. Priestley, C.H.B.; Taylor, R.J. On the Assessment of Surface Heat Flux and Evaporation Using Large-Scale Parameters. *Mon. Weather Rev.* **1972**, *100*, 81–92. [CrossRef]
69. Li, S.; Kang, S.; Zhang, L.; Zhang, J.; Du, T.; Tong, L.; Ding, R. Evaluation of six potential evapotranspiration models for estimating crop potential and actual evapotranspiration in arid regions. *J. Hydrol.* **2016**, *543*, 450–461. [CrossRef]
70. Lu, J.; Sun, G.; McNulty, S.; Amatya, D.M. A comparison of six potential evapotranspiration methods for regional use in the southeastern United States. *JAWRA J. Am. Water Resour. Assoc.* **2005**, *41*, 621–633. [CrossRef]
71. Marasco, D.E.; Culligan, P.J.; McGillis, W.R. Evaluation of common evapotranspiration models based on measure-ments from two extensive green roofs in New York City. *Ecol. Eng.* **2015**, *84*, 451–462. [CrossRef]
72. Koyama, K.; Kikuzawa, K. Geometrical similarity analysis of photosynthetic light response curves, light saturation and light use efficiency. *Oecologia* **2010**, *164*, 53–63. [CrossRef]
73. He, L.; Chen, J.M.; Gonsamo, A.; Luo, X.; Wang, R.; Liu, Y.; Liu, R. Changes in the Shadow: The Shifting Role of Shaded Leaves in Global Carbon and Water Cycles Under Climate Change. *Geophys. Res. Lett.* **2018**, *45*, 5052–5061. [CrossRef]
74. Tang, S.; Chen, J.; Zhu, Q.; Li, X.; Chen, M.; Sun, R.; Zhou, Y.; Deng, F.; Xie, D. LAI inversion algorithm based on directional reflectance kernels. *J. Environ. Manag.* **2007**, *85*, 638–648. [CrossRef]
75. Zhang, X.; Liang, S.; Wang, K.; Li, L.; Gui, S. Analysis of Global Land Surface Shortwave Broadband Albedo From Multiple Data Sources. *IEEE J. Sel. Top. Appl. Earth Obs. Remote Sens.* **2010**, *3*, 296–305. [CrossRef]
76. Duan, Q.; Sorooshian, S.; Gupta, V. Effective and efficient global optimization for conceptual rainfall-runoff models. *Water Resour. Res.* **1992**, *28*, 1015–1031. [CrossRef]
77. Peng, D.; Zhang, X.; Wu, C.; Huang, W.; Gonsamo, A.; Huete, A.R.; Didan, K.; Tan, B.; Liu, X.; Zhang, B. Intercomparison and evaluation of spring phenology products using National Phenology Network and AmeriFlux observations in the contiguous United States. *Agric. For. Meteorol.* **2017**, *242*, 33–46. [CrossRef]

78. Demirel, M.C.; Mai, J.; Mendiguren, G.; Koch, J.; Samaniego, L.; Stisen, S. Combining satellite data and appropriate objective functions for improved spatial pattern performance of a distributed hydrologic model. *Hydrol. Earth Syst. Sci.* **2018**, *22*, 1299–1315. [CrossRef]
79. Mutowo, G.; Mutanga, O.; Masocha, M. Evaluating the Applications of the Near-Infrared Region in Mapping Foliar N in the Miombo Woodlands. *Remote Sens.* **2018**, *10*, 505. [CrossRef]
80. Clevers, J.G.P.W.; Gitelson, A.A. Remote estimation of crop and grass chlorophyll and nitrogen content using red-edge bands on Sentinel-2 and -3. *Int. J. Appl. Earth Observ. Geoinf.* **2013**, *23*, 344–351. [CrossRef]
81. Wang, Z.; Huang, M.; Gong, H.; Li, X.; Zhang, H.; Zhou, X. Increased tropical vegetation respiration is dually induced by El Niño and upper atmospheric warm anomalies. *Sci. Total Environ.* **2022**, *818*, 151719. [CrossRef]
82. Smith, W.K.; Reed, S.C.; Cleveland, C.C.; Ballantyne, A.P.; Anderegg, W.R.L.; Wieder, W.R.; Liu, Y.Y.; Running, S.W. Large divergence of satellite and Earth system model estimates of global terrestrial CO2 fertilization. *Nat. Clim. Chang.* **2016**, *6*, 306–310. [CrossRef]
83. Madani, N.; Kimball, J.S.; Affleck, D.L.R.; Kattge, J.; Graham, J.; van Bodegom, P.M.; Reich, P.B.; Running, S.W. Improving ecosystem productivity modeling through spatially explicit estimation of optimal light use efficiency. *J. Geophys. Res. Biogeosciences* **2014**, *119*, 1755–1769. [CrossRef]
84. Wang, Y.; Li, R.; Hu, J.; Fu, Y.; Duan, J.; Cheng, Y. Daily estimation of gross primary production under all sky using a light use efficiency model coupled with satellite passive microwave measurements. *Remote Sens. Environ.* **2021**, *267*, 112721. [CrossRef]
85. Yuan, W.; Cai, W.; Nguy-Robertson, A.L.; Fang, H.; Suyker, A.E.; Chen, Y.; Dong, W.; Liu, S.; Zhang, H. Uncertainty in simulating gross primary production of cropland eco-system from satellite-based models. *Agric. For. Meteorol.* **2015**, *207*, 48–57. [CrossRef]
86. Loozen, Y.; Rebel, K.T.; Karssenberg, D.; Wassen, M.J.; Sardans, J.; Peñuelas, J.; De Jong, S.M. Remote sensing of canopy nitrogen at regional scale in Mediterranean forests using the spaceborne MERIS Terrestrial Chlorophyll Index. *Biogeosciences* **2018**, *15*, 2723–2742. [CrossRef]
87. Baldocchi, D. Measuring fluxes of trace gases and energy between ecosystems and the atmosphere—The state and future of the eddy covariance method. *Glob. Chang. Biol.* **2014**, *20*, 3600–3609. [CrossRef]
88. Rousel, J.; Haas, R.; Schell, J.; Deering, D. Monitoring vegetation systems in the great plains with ERTS. In Proceedings of the Third Earth Resources Technology Satellite—1 Symposium, NASA SP-351, Washington, DC, USA, 10–15 December 1974; pp. 309–317.
89. Jordan, C.F. Derivation of Leaf-Area Index from Quality of Light on the Forest Floor. *Ecology* **1969**, *50*, 663–666. [CrossRef]
90. Gitelson, A.A.; Kaufman, Y.J.; Merzlyak, M.N. Use of a green channel in remote sensing of global vegetation from EOS-MODIS. *Remote Sens. Environ.* **1996**, *58*, 289–298. [CrossRef]
91. Rondeaux, G.; Steven, M.; Baret, F. Optimization of soil-adjusted vegetation indices. *Remote Sens. Environ.* **1996**, *55*, 95–107. [CrossRef]
92. Penuelas, J.; Frederic, B.; Filella, I. Semi-Empirical Indices to Assess Carotenoids/Chlorophyll-a Ratio from Leaf Spectral Reflectance. *Photosynthetica* **1995**, *31*, 221–230.
93. Zarco-Tejada, P.J.; Berjón, A.; López-Lozano, R.; Miller, J.R.; Martín, P.; Cachorro, V.; González, M.R.; De Frutos, A. Assessing vineyard condition with hyperspectral indices: Leaf and canopy reflectance simulation in a row-structured discontinuous canopy. *Remote Sens. Environ.* **2005**, *99*, 271–287. [CrossRef]
94. Gitelson, A.A.; Viña, A.; Arkebauer, T.J.; Rundquist, D.C.; Keydan, G.; Leavitt, B. Remote estimation of leaf area index and green leaf biomass in maize canopies. *Geophys. Res. Lett.* **2003**, *30*, 1248. [CrossRef]
95. Jiang, Z.; Huete, A.R.; Didan, K.; Miura, T. Development of a two-band enhanced vegetation index without a blue band. *Remote Sens. Environ.* **2008**, *112*, 3833–3845. [CrossRef]
96. Gitelson, A.A. Wide Dynamic Range Vegetation Index for Remote Quantification of Biophysical Characteristics of Vegetation. *J. Plant Physiol.* **2004**, *161*, 165–173. [CrossRef]
97. Peng, Y.; Gitelson, A.A. Application of chlorophyll-related vegetation indices for remote estimation of maize productivity. *Agric. For. Meteorol.* **2011**, *151*, 1267–1276. [CrossRef]
98. Chen, J.M. Evaluation of Vegetation Indices and a Modified Simple Ratio for Boreal Applications. *Can. J. Remote Sens.* **1996**, *22*, 229–242. [CrossRef]
99. Metternicht, G. Vegetation indices derived from high-resolution airborne videography for precision crop management. *Int. J. Remote Sens.* **2003**, *24*, 2855–2877. [CrossRef]
100. Vincini, M.; Frazzi, E.; Alessio, P. *Angular Dependence of Maize and Sugar Beet VIs from Directional CHRIS/Proba Data*; ESRIN: Frasati, Italy, 2006.
101. Lichtenthaler, H.K.; Lang, M.; Sowinska, M.; Heisel, F.; Miehé, J.A. Detection of Vegetation Stress Via a New High Resolution Fluorescence Imaging System. *J. Plant Physiol.* **1996**, *148*, 599–612. [CrossRef]
102. Huete, A.R.; Liu, H.Q.; Batchily, K.V.; van Leeuwen, W. A comparison of vegetation indices over a global set of TM images for EOS-MODIS. *Remote Sens. Environ.* **1997**, *59*, 440–451. [CrossRef]
103. Haboudane, D.; Miller, J.R.; Pattey, E.; Zarco-Tejada, P.J.; Strachan, I.B. Hyperspectral vegetation indices and novel algorithms for predicting green LAI of crop canopies: Modeling and validation in the context of precision agriculture. *Remote Sens. Environ.* **2004**, *90*, 337–352. [CrossRef]

104. Badgley, G.; Field, C.B.; Berry, J.A. Canopy near-infrared reflectance and terrestrial photosynthesis. *Sci. Adv.* **2017**, *3*, e1602244. [CrossRef]
105. Camps-Valls, G.; Campos-Taberner, M.; Moreno-Martínez, A.; Walther, S.; Duveiller, G.; Cescatti, A.; Mahecha, M.D.; Muñoz-Marí, J.; García-Haro, F.J.; Guanter, L.; et al. A unified vegetation index for quantifying the terrestrial biosphere. *Sci. Adv.* **2021**, *7*, eabc7447. [CrossRef] [PubMed]
106. Gamon, J.A.; Huemmrich, K.F.; Wong, C.Y.S.; Ensminger, I.; Garrity, S.; Hollinger, D.Y.; Noormets, A.; Peñuelas, J. A remotely sensed pigment index reveals photosynthetic phenology in evergreen conifers. *Proc. Natl. Acad. Sci. USA* **2016**, *113*, 13087–13092. [CrossRef] [PubMed]
107. Takagi, K.; Kotsuka, C.; Fukuzawa, K.; Kayama, M.; Makoto, K.; Watanabe, T.; Nomura, M.; Fukazawa, T.; Takahashi, H.; Hojyo, H.; et al. Allometric Relationships and Carbon and Nitrogen Contents for Three Major Tree Species (Quercus crispula, Betula ermanii, and Abies sachalinensis) in Northern Hokkaido, Japan. *Eurasian J. For. Res.* **2010**, *13*, 1–7.
108. Klopatek, J.M.; Barry, M.J.; Johnson, D.W. Potential canopy interception of nitrogen in the Pacific Northwest, USA. *For. Ecol. Manag.* **2006**, *234*, 344–354. [CrossRef]